Global Biogeochemical Cycles

RESEARCH ARTICLE
10.1029/2020GB006684

Stable Carbon Isotopes Suggest Large Terrestrial Carbon Inputs to the Global Ocean

Eun Young Kwon[1,2], Tim DeVries[3,4], Eric D. Galbraith[5,6,7], Jeomshik Hwang[8], Guebuem Kim[8], and Axel Timmermann[1,2]

[1]Center for Climate Physics, Institute for Basic Science, Busan, South Korea, [2]Pusan National University, Busan, South Korea, [3]Department of Geography, University of California, Santa Barbara, CA, USA, [4]Earth Research Institute, University of California, Santa Barbara, CA, USA, [5]ICREA, Pg. Lluís Companys 23, Barcelona, Spain, [6]Institut de Ci encia i Tecnologia Ambientals (ICTA) and Department of Mathematics, Universitat Autonoma de Barcelona, Barcelona, Spain, [7]Now at Earth and Planetary Science, McGill University, Montreal, Canada, [8]School of Earth and Environmental Sciences/Research Institute of Oceanography, Seoul National University, Seoul, South Korea

Key Points:

- Total terrestrial carbon input to the global ocean is about two times larger than riverine inputs alone
- Most of the non-riverine coastal margin carbon inputs occur in the Indian and Pacific Oceans
- The terrestrial carbon input is largely balanced by an efflux to the atmosphere, 40% of which occurs in poorly monitored coastal regions

Supporting Information:

Supporting Information may be found in the online version of this article.

Correspondence to:

E. Y. Kwon,
ekwon957@gmail.com

Citation:

Kwon, E. Y., DeVries, T., Galbraith, E. D., Hwang, J., Kim, G., & Timmermann, A. (2021). Stable carbon isotopes suggest large terrestrial carbon inputs to the global ocean. *Global Biogeochemical Cycles*, *35*, e2020GB006684. https://doi.org/10.1029/2020GB006684

Received 28 MAY 2020
Accepted 6 MAR 2021

Abstract The transport of carbon from land to ocean, via rivers, groundwater, and aerosols, is an important component of the global carbon cycle that must be known to accurately assess anthropogenic CO_2 storage on land and in the ocean. Current global carbon cycle budgets have adopted terrestrial carbon inputs to the ocean ranging from 0.5 GtC/yr to 0.9 GtC/yr, derived mainly from estimates of riverine fluxes. However, these budgets ignore the terrestrial carbon inputs from coastal ecosystems and through submarine groundwater discharge (collectively referred to as coastal margin inputs in this study) due to difficulties in making global assessments. Using a numerical model and globally distributed ocean observations of stable carbon isotopes, we estimate terrestrial carbon inputs to the ocean at 1.4 ± 0.5 GtC/yr, with 95% of the coastal margin inputs (0.8 ± 0.5 GtC/yr) occurring in the Pacific and Indian Oceans. This terrestrial carbon flux is largely balanced by an efflux to the atmosphere of 1.2 ± 0.5 GtC/yr, 40% of which occurs in poorly monitored coastal regions and may have been overlooked in previous observation-based global estimates. Our results suggest more dynamic cycling of carbon in the land-ocean transition zone than previously thought, and that rivers may not be the only important pathway for terrestrial carbon to the ocean.

Plain Language Summary The transfer of carbon from the land to the ocean is an important part of the global carbon cycle, but its magnitude is not well known. By combining global oceanic compilations of observed stable carbon isotopes with an ocean inverse model, we provide new constraints on terrestrial carbon inputs to the ocean within the overall cycling of carbon in the atmosphere-land-ocean system. Our results show that the terrestrial carbon flux to the ocean could be up to two times larger than previously believed. The results highlight the importance of vegetated coastal margins that transport carbon into the ocean, which are often overlooked in biogeochemical cycles and have important implications for the global carbon cycle and the fate of anthropogenic CO_2.

1. Introduction

Accurately determining the carbon exchange between the atmosphere, land, and ocean over preindustrial and industrial times is critical for understanding how humans have perturbed the Earth's carbon cycle (Resplandy et al., 2018). The prevailing understanding of the global carbon cycle suggests that in preindustrial times about 0.9 GtC/yr was transferred from land to the ocean (Cole et al., 2007; Meybeck, 1993), of which 0.2 GtC/yr was buried in marine sediments (Sarmiento & Sundquist, 1992) and 0.7 GtC/yr outgassed to the atmosphere (Ciais et al., 2013). Superimposed on these preindustrial carbon fluxes are anthropogenic perturbations consisting of a 0.1 GtC/yr increase in the carbon flux from land to ocean via rivers (Regnier et al., 2013) and the oceanic uptake of anthropogenic CO_2 of 2.3 ± 0.7 GtC/yr as of the 2000s (Sarmiento & Gruber, 2006). Taken together, the inferred net oceanic CO_2 uptake of 1.6 ± 0.7 GtC/yr (consisting of 0.7 GtC/yr outgassing of natural CO_2 and 2.3 ± 0.7 Gt/yr anthropogenic CO_2 uptake) is considered to be in agreement with estimates of the contemporary air-sea CO_2 flux derived from the observed oceanic partial pressure of CO_2 (pCO_2) (1.4 ± 0.5 GtC/yr as of 2000) (Landschützer et al., 2017) and ocean inverse models (1.7 ± 0.4 GtC/yr as of 1995–2000) (Gruber et al., 2009). However, this understanding of carbon fluxes

is based on limited observations at the world's major river mouths (Cole et al., 2007) and in the coastal ocean (Laruelle et al., 2013, 2014), and therefore potentially misses carbon fluxes occurring in the world's coastal oceans away from major river mouths and in poorly sampled coastal regions (Bauer et al., 2013; Duarte, 2017).

Along the coastal margins, carbon is exported laterally from estuaries, mangroves, salt marshes, and intertidal freshwater forests (Abril et al., 2013; Alongi & Mukhopadhyay, 2014; Bauer et al., 2013; Chen et al., 2018; Cole et al., 2007; Maher et al., 2013; Moore, 2010; Rosentreter et al., 2018; Szymczycha et al., 2014). These coastal ecosystems can fix CO_2 from the atmosphere, and supply carbon to the ocean either by direct export of organic materials (Duarte, 2017) or through submarine groundwater discharge (SGD) (Chen et al., 2018). A large fraction of SGD is driven by tides, waves, and density-driven pressure gradients that pump seawater into coastal aquifers and sediments, where the mixture of meteoric and saline groundwater loads both organic and inorganic carbon derived from soils and vegetation in coastal areas (Moore, 2010). Previous studies estimated SGD-driven export of 0.19–0.84 GtC/yr (Cole et al., 2007; Szymczycha et al., 2014) and the export from coastal vegetation of 0.1–1.9 GtC/yr (Duarte, 2017). The large uncertainties in these estimates reflect challenges associated with scaling regional assessments of carbon fluxes in the highly complex and heterogeneous coastal margins to the global scale. Reconciling these potentially large coastal margin carbon fluxes with the balanced carbon budget is a significant challenge for the global carbon cycle community, and new sources of information are needed that can shed light on the global magnitude of carbon fluxes from land into the ocean.

Stable carbon isotopes potentially provide a strong geochemical constraint on terrestrial carbon fluxes to the ocean. Carbon derived from terrestrial plants is highly depleted in ^{13}C ($\delta^{13}C$ values ranging from −34‰ to −10‰) (Marwick et al., 2015; Peterson & Fry, 1987) compared to seawater ($\delta^{13}C$ values ranging from −1‰ to 2‰) (Schmittner et al., 2017), where $\delta^{13}C$ is defined as $\delta^{13}C = (({}^{13}C/{}^{12}C)_{sample}/({}^{13}C/{}^{12}C)_{standard} - 1) \times 10^3$ with the Vienna Pee Dee Belemnite standard. Previous studies have used the isotopic signature of organic and inorganic carbon in seawater to determine terrestrial carbon fluxes to the ocean on regional scales (Hedges et al., 1997). Once exported to the ocean, terrestrial organic carbon is respired by heterotrophic organisms, converting it to dissolved inorganic carbon (DIC) with low $\delta^{13}C$ values on timescales spanning from a few years (Anderson et al., 2019; Manizza et al., 2009) to a century (Meybeck, 1993). DIC derived from terrestrial sources is also depleted in ^{13}C because a large fraction of it originates from the respiration of land plant material in terrestrial water reservoirs, rivers, and soils (Marwick et al., 2015; Peterson & Fry, 1987). The strong imprint of terrestrial carbon fluxes on the global oceanic $^{13}C/^{12}C$ distributions (Quay et al., 2003; Sonnerup & Quay, 2012), together with the long air-sea $\delta^{13}C$ equilibrium timescale of a decade (Galbraith et al., 2015) that exceeds the coast-open ocean water exchange timescales of days to years (Liu et al., 2019), can serve as a constraint on the magnitude of land-to-ocean carbon fluxes on basin to global scales. However, constraining the land-derived carbon export requires accounting for the convolved effects of ocean circulation, marine biological cycling, and air-sea exchange (Jahn et al., 2015; Krakauer et al., 2006; Lynch-Stieglitz et al., 1995; Schmittner et al., 2013), all of which are integrated over multi-millennial timescales and superimposed by the anthropogenic input of low $\delta^{13}C$ carbon dioxide from fossil fuels (Eide et al., 2017; Gruber et al., 1999; Sonnerup et al., 2007).

Here, we develop a numerical model of the global oceanic cycling of stable carbon isotopes, and use available observations of DIC (Lauvset et al., 2016) and the $\delta^{13}C$ of DIC (Schmittner et al., 2017) to estimate the total flux of terrestrial carbon to the ocean. The total flux of terrestrial carbon includes prescribed riverine and airborne carbon inputs (Lamarque et al., 2010; Mayorga et al., 2010; Meybeck & Ragu, 2012) and additional sources of terrestrial carbon to the ocean through SGD and from coastal vegetation, which collectively we refer to as "coastal margin" inputs. We simultaneously optimize the magnitude and $\delta^{13}C$ value of the globally integrated coastal margin inputs, and the model parameters controlling air-sea CO_2 exchange and inorganic carbon burial into marine sediments, to determine the global input of terrestrial carbon to the ocean that is consistent with stable carbon isotope observations. We furthermore explore the uncertainty associated with our estimates using a series of sensitivity experiments and Monte Carlo simulations that address several key model assumptions and uncertainties.

Although we provide a first global estimate for the terrestrial carbon inputs and the $\delta^{13}C$ signature of the coastal margin inputs, our estimates come with several caveats. First, since the global database of DIC and

the $\delta^{13}C$ of DIC only constrains total terrestrial carbon inputs, any uncertainties in the prescribed riverine and airborne carbon inputs can propagate into the estimated coastal margin inputs. Therefore, the total terrestrial carbon inputs have a lower uncertainty than the estimates for the coastal margin inputs alone. Second, our estimate for terrestrial carbon inputs is based on the amount of land-originated carbon that best explains the large-scale (>200 km) distributions of carbon isotopes in the ocean. The model does not fully resolve coastal or shelf processes, nor does it include a portion of land-derived organic carbon that is buried in coastal sediments (Bianchi et al., 2017; Cai, 2011) without affecting large-scale carbon isotope distributions. Finally, our model assumes a preindustrial steady-state carbon cycle, and thus any imbalanced fluxes (e.g., transient carbon burial in marine sediments due to slow adjustment to sea level changes) (Cartapanis et al., 2018; Milliman, 1993) are not captured in our estimates.

This study is organized as follows: In Section 2, we describe the ocean carbon isotope model and the model parameters to be optimized. In Section 3, we describe the optimization methods and the carbon isotope observations used for the optimization. In Section 4, we present our optimal estimates for the carbon fluxes, and show how the optimal model is consistent or inconsistent with previous estimates of the air-sea $\delta^{13}C$ disequilibrium of CO_2 and the globally integrated air-sea CO_2 exchange in the open ocean and coastal ocean. In Section 5, we discuss the uncertainties of the model and the estimated carbon fluxes. In Section 6, we summarize our results and offer concluding remarks.

2. The Ocean Carbon Cycle Model

2.1. The Ocean Circulation and Biogeochemistry Model

We use the observationally constrained circulation inverse model (OCIM) of DeVries (2014) as a basis for building our stable carbon isotope model. The OCIM is based on a simplified version of the primitive equations using hydrostatic, rigid lid, and Boussinesq approximations (DeVries & Primeau, 2011). Nonlinear momentum advection is ignored, following the large-scale geostrophic approximation (Maier-Reimer et al., 1993), but its effects are parameterized by optimized corrections to the horizontal momentum equations. The horizontal resolution of the model is $2° \times 2°$ and the vertical resolution ranges from 36 m near the top to 633 m near the bottom with a total of 24 vertical layers. Sub-grid scale mixing processes are parameterized with the isopycnal and diapycnal diffusivities of 10^3 m^2 s^{-1} and 10^{-5} m^2 s^{-1}, respectively. The KPP scheme (Large et al., 1994) is used to parameterize vertical mixing in the surface mixed layer. The dynamical model assimilates observations of temperature, salinity, CFC-11 and radiocarbon, as well as reanalysis data of heat and freshwater fluxes, sea-surface height and wind stress to produce ocean transport estimates that are optimally consistent with the observations. The circulation model was previously used to simulate the oceanic uptake and storage of anthropogenic carbon, which was shown to be consistent with previous independent estimates (DeVries, 2014).

We embed a simple ocean biogeochemistry model into the OCIM. The biogeochemistry model is based on the OCMIP-II protocol (Najjar et al., 2007) and is similar to the one used in Kwon et al. (2012) and Kwon and Primeau (2008). There are six prognostic biogeochemical tracers, which include phosphate (PO_4), semi-labile dissolved organic phosphorus (DOP), alkalinity, $DI^{12}C$, $DI^{13}C$, and semi-labile dissolved organic carbon (DOC) (Note that $DO^{12}C$ is linearly scaled with DOP with a constant stoichiometric ratio of C:P and hence is not a prognostic tracer in the model whereas $DO^{13}C$ is a prognostic tracer). The isotope fractionation factors used in this study are from previous lab- and field-based studies that determined the fractionation during air-sea gas exchange (Zhang et al., 1995) and during marine photosynthesis (Goericke & Fry, 1994). Full model equations are provided in Text S1.

The circulation and biogeochemistry models are all based on the annually averaged climatological fields and fluxes. The lack of explicit representation of the seasonal cycle is an important caveat of this study, because the annual mean ocean circulation model that best fits the observations inevitably accompanies sea surface temperatures (SST) that are biased toward the seasons where deep and intermediate water form and subduct into the ocean's interior (DeVries, 2014; DeVries & Primeau, 2011). To address this issue, our "Standard" model (Table S1) replaces the modeled SST field with the annual mean SST from the Met Office Hadley Center's sea surface temperature data set (HadISST) (Rayner et al., 2003) when calculating the equilibrium fractionation factors for carbon isotopes, but retains the model SST when calculating CO_2

solubility. The reasoning behind this is that the equilibrium fractionations for the $\delta^{13}C$ of DIC are likely to be influenced by the annual mean SST due to the long (~10 years) air-sea equilibrium timescales of $\delta^{13}C$-DIC (Galbraith et al., 2015). On the other hand, the solubility of CO_2 is more heavily influenced by the SST averaged over the water mass subduction period (winter), due to the shorter air-sea equilibrium timescales of ~6 months for ^{12}C. We explore the influence of these assumptions with sensitivity experiments using different SST fields in the model (Text S2 for further details).

2.2. River and Aerosol Carbon Inputs

The model includes the air-borne deposition of organic and black carbon (Lamarque et al., 2010) and the estimates of riverine transport of organic and inorganic carbon (Mayorga et al., 2010; Meybeck & Ragu, 2012). Three forms of carbon are exported from land to ocean via rivers and through aerosol deposition: DOC and DIC by rivers, and particulate organic carbon (POC) by rivers and aerosols. The riverine DOC and POC exports are obtained from the second phase of the Global Nutrient Export from Watersheds (NEWS2) model (Mayorga et al., 2010) which integrate to 0.17 GtC/yr and 0.14 GtC/yr, respectively. The riverine DIC flux is computed using the GEMS-GLORI database (Meybeck & Ragu, 2012) that contains DIC measurements for 251 major rivers. For rivers that have no DIC measurements (n = 1,162 rivers total), we assume a DIC concentration of 770 mmol/m^3, based on the log-transformed average of DIC measurements in the GEMS-GLORI database. This simplification does not account for spatial dependency of DIC fluxes on rock types (Lacroix et al., 2020), but yields a globally integrated riverine DIC flux of 0.30 GtC/yr, similar to 0.32 GtC/yr obtained when accounting for this factor (Ludwig et al., 1996). The riverine carbon sources are assumed to be time-invariant and occur in the ocean grids adjacent to river mouths at the sea surface (Figure S1). The atmospheric deposition of organic and black carbon follows Lamarque et al. (2010) which varies spatially and temporally. The globally integrated airborne fluxes are considerably smaller than the riverine fluxes, amounting to only 0.01 GtC/yr as of 1780 and 0.02 GtC/yr as of 2016.

The isotopic compositions ($\delta^{13}C$) and oceanic cycling of the different forms of terrestrial carbon are distinct in the model. The isotopic signatures of riverine carbon fluxes are globally uniform and fixed at $\delta^{13}C = -27‰$ for DOC, $\delta^{13}C = -30‰$ for POC, and $\delta^{13}C = -15‰$ for DIC following Marwick et al. (2015) and Peterson and Fry (1987) (see Text S2 for the model sensitivity to the prescribed $\delta^{13}C$ values). Once exported to the ocean from river mouths, riverine DOC is transported by ocean circulation and decomposed back to DIC with an e-folding time of 8 years (Manizza et al., 2009). Discharged riverine POC is assumed to be deposited in the bottom layers at river mouths and completely decomposed to DIC there. Due to this assumption, refractory POC that is exported to the open ocean and buried in marine sediments (Blair & Aller, 2012; Galy et al., 2015) is not represented in the model. The cycling of airborne POC ($\delta^{13}C = -30‰$) is highly uncertain, so we make an assumption that the airborne POC flux sinks vertically to the bottom layer of the ocean where it is remineralized completely. Riverine DIC is mixed with oceanic DIC as soon as it is discharged, and is then subject to biological cycling, air-sea gas exchange, chemical reactions, and sedimentary burial. We do not consider spatial variability in the $\delta^{13}C$ values of river-derived carbon, which could vary depending on the vegetation and rock types in river catchments and the influence of petrogenic organic carbon (Galy et al., 2015; Ludwig et al., 1996; Murgulet et al., 2018). These variations are likely important for local-scale carbon isotope budgets, but are less important for the global and basin-scale budgets considered in our study.

2.3. Coastal Margin Carbon Inputs

Relative to the riverine and airborne inputs to the ocean, the magnitude and geographic distributions of coastal margin carbon inputs are highly uncertain. Because SGD-driven carbon inputs and the lateral carbon export from coastal vegetation are not independent of each other, we lump these two carbon sources together as a single carbon source, collectively called "coastal margin" carbon inputs. The depth range for SGD has been previously constrained as the top ~200 m of the water column (Kwon et al., 2014), consistent with the fact that most of coastal aquifers outcrop within the continental shelf (Taniguchi et al., 2002). Moreover, the coastal margin carbon inputs are likely to be in a form of DIC or easily degradable organic carbon (Abril et al., 2013; Cai, 2011; Chen et al., 2018; Dorsett et al., 2011; Maher et al., 2013). Therefore, we assume that coastal margin carbon inputs occur as DIC within the top 217 m (top five vertical layers) in

model ocean grid cells adjacent to the land grid cells, excluding those around Antarctica. The coastal margin-derived DIC is then assumed to undergo the same physical and biogeochemical processes as riverine DIC, except that the coastal margin $\delta^{13}C$ value is optimized instead of being prescribed in the model. Some of the assumptions made for the coastal margin inputs, as well as those for the riverine carbon inputs, are explored in Section 5.3 and in Text S2.

2.4. Carbon Burial in Sediments

We implement a simple steady-state representation for the sedimentary burial of inorganic carbon. A uniform DIC flux is removed from the ocean bottom layer where waters are supersaturated with respect to calcite. The saturation state with respect to calcite is determined using the GLobal Ocean Data Analysis Project (GLODAPv2) data (Lauvset et al., 2016), which shows continental shelves and the Atlantic mid ocean ridges as major regions of $CaCO_3$ burial. This carbonate burial term is needed in order to balance the carbon export originating from weathering of carbonate minerals on land (Cartapanis et al., 2018; Milliman, 1993). The model does not explicitly represent the burial of organic carbon, but the potential effect of organic carbon burial on our estimates, as well as the uncertainty arising from the steady-state assumption, are discussed in Text S2.

2.5. Other Considerations

No terrestrial sources of PO_4 are assumed in the model except for an idealized experiment using riverine PO_4 inputs (Mayorga et al., 2010) (see Text S2). The ocean alkalinity is not affected by the terrestrial carbon fluxes, but instead is fixed at the model solution optimized against the contemporary observations (Lauvset et al., 2016) throughout this study. Sub-aerial volcanism is also not explicitly simulated in the model, but its isotopic signature is implicitly accounted for in the atmospheric composition (which is imposed as a boundary condition). Because sub-aerial volcanism is mostly balanced by silicate rock weathering (Burton & Sawyer, 2013), whose isotopic signature imprints on the riverine DIC fluxes, the isotopic effects of these processes are implicitly included in the model.

2.6. Model Simulations

A valuable feature of our model is that the ocean biogeochemistry model directly solves for a preindustrial steady-state solution using Newton's method instead of taking a traditional time-stepping approach (Kwon & Primeau, 2008). With this technique, steady-state solutions for all biogeochemical tracers are obtained for a given ocean circulation field within a few minutes of computation using a single processor computer. Starting from this preindustrial steady-state solution, we integrate the model's governing equations from 1780 to 2016 using the historical atmospheric CO_2 change (see Section 3.1), which takes several hours of computing time. This computational efficiency allows us to perform a formal optimization experiment that requires hundreds of iterations for an optimal solution, and to perform additional experiments to explore the sensitivity of our model to various assumptions (Section 5 and Text S2). The ocean circulation and biological source/sink are held fixed in all simulations at the present-day climatological-means. Hence, the model simulations should be compared with the climatological-mean values from observations.

2.7. Model Parameters to be Optimized

We optimize all of the model parameters relevant to the coastal margin carbon input, and the carbon exchange between the ocean and atmosphere and between the ocean and marine sediments, which include: (i) a parameter representing the input of carbon to the ocean from coastal margins (excluding Antarctica), which together with the prescribed riverine and airborne fluxes, captures the total carbon fluxes from land to ocean during the preindustrial era, (ii) a scaling parameter for the temporal evolution of the coastal margin carbon fluxes to the ocean from 1780 to 2016, assumed to be linearly related to the atmospheric growth of CO_2 (Keeling et al., 2005; MacFarling Meure et al., 2006), (iii) two parameters representing the preindustrial $\delta^{13}C$ value for coastal margin fluxes and its temporal change during the industrial time, (iv) a linear scaling parameter to the air-sea CO_2 transfer velocity formulated by Wanninkhof (1992), and (v) a

parameter, which dictates the rate of sedimentary burial fluxes of inorganic carbon in the ocean (see Text S1 for model formulations with the parameters).

These parameters are optimized simultaneously. The simultaneous consideration of the key components of the carbon cycle is essential for this study, because the carbon fluxes and some of the model parameters are correlated to each other. Another advantage of the simultaneous consideration is that our optimized parameter values can be compared against estimates from previous independent studies to ensure that our optimization gives reasonable results, while at the same time allowing for more degrees of freedom in the optimization.

3. Carbon Isotope Data and Model Optimization

3.1. Observed Atmospheric CO_2 and the $\delta^{13}C$ of CO_2

The atmospheric $^{12}CO_2$ follows the industrial change, according to the spline fits to the ice core measurements made at Law Dome, Antarctica from 1780 to 1958 (MacFarling Meure et al., 2006) and to the direct atmospheric measurements made at Mauna Loa observatory and South Pole from 1959 to 2016 (Keeling et al., 2005). Annual means are calculated using the smoothed monthly mean atmospheric $^{12}CO_2$ data from the two stations. We average the two annual-mean values to obtain the global-mean atmospheric CO_2. For the isotopic composition of atmospheric CO_2, we first compute the annual-mean $\delta^{13}C$ values using the smoothed monthly mean data from Mauna Loa observatory and South Pole over the time period of 1980–2016, and then we take the average of the two stations to represent the global-mean values. In order to interpolate the atmospheric $\delta^{13}C$ observation to the times earlier than 1980, we combine the pairs of the atmospheric $^{12}CO_2$ and the $\delta^{13}C$ of atmospheric CO_2 for the time period of 1980–2016 with preindustrial mean values of $^{12}CO_2{}^{air} = 280$ ppm and $\delta^{13}C = -6.5‰$ (Rubino et al., 2013) for a year of 1780. The total 38 pairs are used to determine the second order polynomial function relating the atmospheric $\delta^{13}C$ with $^{12}CO_2$, i.e., $\delta^{13}C^{air} = 2.26–0.0417 \times (^{12}CO_2{}^{air}) + 3.75 \times 10^{-5} \times (^{12}CO_2{}^{air})^2$, where $(^{12}CO_2{}^{air})$ is atmospheric CO_2 in ppm and $\delta^{13}C^{air}$ is the $\delta^{13}C$ of atmospheric CO_2 in ‰, which fits the observations well with $R^2 > 0.99$.

3.2. Observations of the $\delta^{13}C$ of DIC

We use a global database of the water-column $\delta^{13}C$ of DIC compiled by Schmittner et al. (2017). The data covers major parts of the global ocean with a time span between 1972 and 2016. To facilitate the model-observation comparison, we map the observed $\delta^{13}C$ of DIC onto our 2° × 2° model grid cells by averaging all data points within each grid cell at each year. This gridding process condenses the total number of observation points from $n = 26{,}750$ to $n = 17{,}864$. As a quality control, we remove the observation grid cells with a standard error exceeding 0.05‰, further reducing the number of observation grid cells by 11% to $n = 15{,}932$. With this exclusion, 75% of the observation points have standard errors less than 0.01‰. To obtain a climatological mean distribution, we average the gridded data over time such that each grid cell has an averaged year of data collection and an averaged $\delta^{13}C$ value (Figures 1a and 1b). This temporal averaging, resulting in the number of grid cells $n = 14{,}561$, facilitates the comparison with the model that has no seasonal variability. Finally, also due to the model's inability to resolve the seasonal cycle, we exclude observations falling within the winter mixed layer, determined using the World Ocean Atlas 2013 (WOA) database (Garcia et al., 2014). The resulting subsurface grid cells ($n = 12{,}635$) are used for model optimization.

Although not used for constraining the model-based estimates, surface measurements of $\delta^{13}C$-DIC from the same global database (Schmittner et al., 2017) are used when estimating the isotopic disequilibrium of CO_2. The preprocessing procedure for surface measurements is the same as the one for subsurface measurements except that we do not remove the observation grid cells with a standard error exceeding 0.05 ‰ due to large seasonal variability in high-latitude surface $\delta^{13}C$ values (Becker et al., 2018; Gruber et al., 1998; Quay et al., 2017; Racapé et al., 2010).

It is important to keep in mind that uncertainties on individual $\delta^{13}C$-DIC values are on the order of 0.1‰–0.2‰ (Schmittner et al., 2013). The averaging and quality-control that we applied to the data can reduce but not eliminate these uncertainties, especially those that are due to intercalibration issues. Thus, the model-observations misfits of ∼0.19‰ (see below) could be partly due to observational errors, rather than

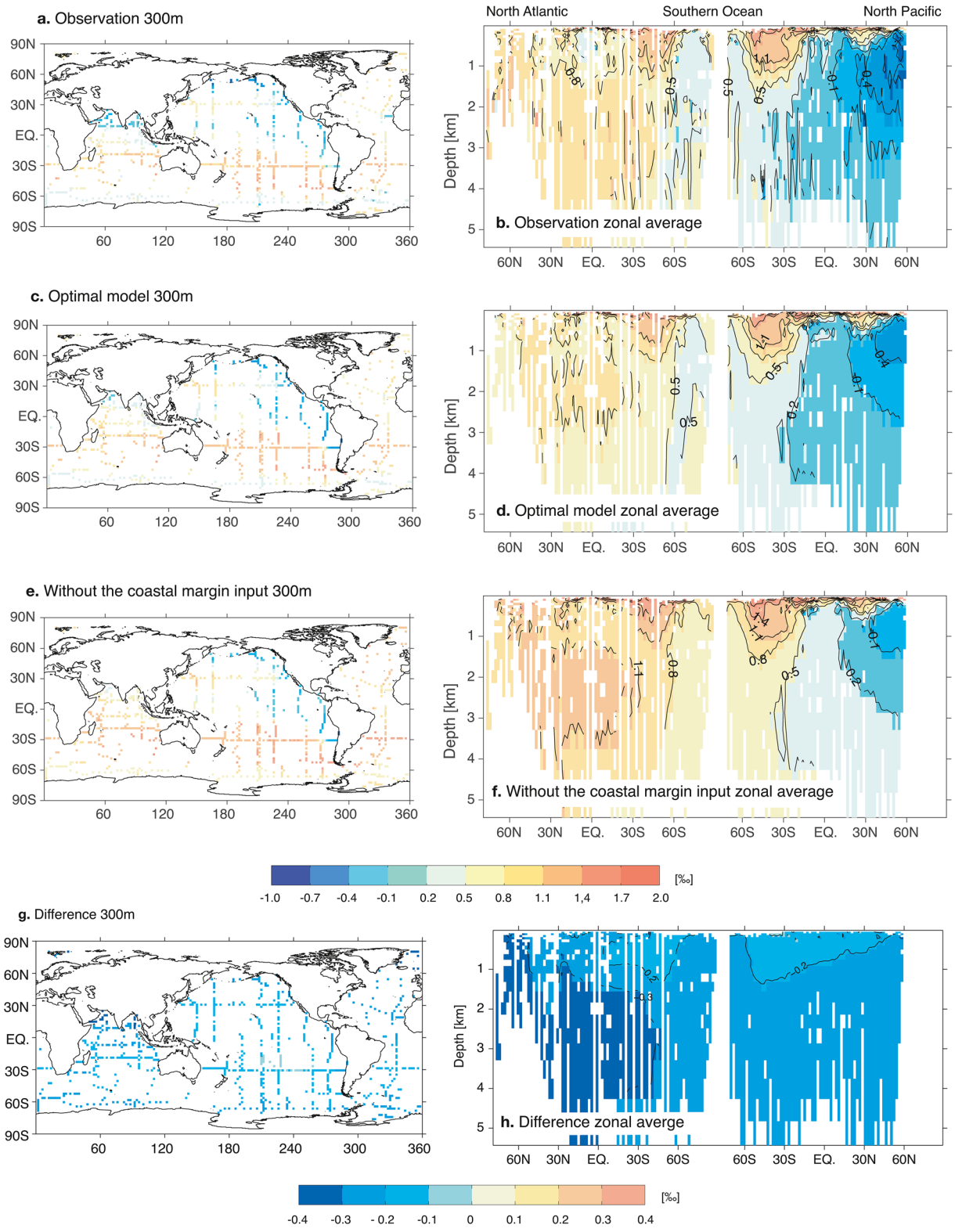
a. Observation 300m
North Atlantic
Southern Ocean
North Pacific
b. Observation zonal average
Depth [km]
c. Optimal model 300m
d. Optimal model zonal average
e. Without the coastal margin input 300m
f. Without the coastal margin input zonal average
[‰]
-1.0 -0.7 -0.4 -0.1 0.2 0.5 0.8 1.1 1,4 1.7 2.0
g. Difference 300m
h. Difference zonal averge
-0.4 -0.3 - 0.2 -0.1 0 0.1 0.2 0.3 0.4
90N 60N 30N EQ. 30S 60S 90S
60 120 180 240 300 360
60N 30N EQ. 30S 60S 60S 30S EQ. 30N 60N

model errors. Nonetheless, for purposes of this study we assume that the observations, when suitably averaged, can accurately capture the true large-scale distribution of δ^{13}C-DIC in the ocean, and interpret the large-scale misfits between the model and observations as due to model imperfections.

3.3. Model Optimization

Our optimization takes two steps. First, we use the globally gridded datasets of PO_4, alkalinity and $DI^{12}C$ to optimize ocean biogeochemical model parameters following Kwon and Primeau (2008). The PO_4 data is taken from the WOA (Garcia et al., 2014) and the alkalinity and $DI^{12}C$ data are adopted from the GLODAPv2 (Lauvset et al., 2016). The gridded climatological mean data are linearly interpolated onto our model grid cells to allow direct comparisons with model solutions. We optimize all of the uncertain biogeochemistry model parameters simultaneously using a formal optimization algorithm implemented in FMINSEARCH in MATLAB (i.e., the unconstrained Nelder-Mead simplex direct search method of Lagarias et al., 1998). The resulting model solutions have volume-weighted root mean squared errors (RMSEs) of 0.18 $\mu molkg^{-1}$ for PO_4, 14 $\mu molkg^{-1}$ for alkalinity, and 20 $\mu molkg^{-1}$ for $DI^{12}C$. We neglect terrestrial carbon inputs in this step because they have very small effects on the oceanic storage and gradients of $DI^{12}C$, relative to biogeochemical processes.

In the second step of our optimization, we fix the biogeochemical parameters at the optimal values found in the first step, and use the observations of $DI^{12}C$ (Lauvset et al., 2016) and the δ^{13}C of DIC (Schmittner et al., 2017) to optimize the parameters listed in Section 2.7. The δ^{13}C in DIC provides the strongest constraint on land-to-ocean carbon fluxes, because the diluting effect on the δ^{13}C of DIC by terrestrial carbon inputs (Quay et al., 2003; Sonnerup & Quay, 2012) is largely balanced by the oceanic enrichment of δ^{13}C during air-sea CO_2 exchange (Lynch-Stieglitz et al., 1995; Schmittner et al., 2013). Stable carbon isotopes are also best suited to constrain the land-derived carbon fluxes to the ocean due to slow air-sea equilibrium timescales that allow its isotopic signature to be imprinted in the large-scale distribution of δ^{13}C-DIC in the open ocean. On the other hand, $DI^{12}C$ provides a weak but complementary constraint on the terrestrial carbon inputs to the ocean and the oceanic carbon budget due to a relatively short air-sea equilibrium timescale (Galbraith et al., 2015) and missing isotopic fractionation effects.

The cost function, a function of the model parameters, is written as

$$\mathrm{CF} = 0.5\frac{\sum \mathrm{vol}\cdot\left(\delta^{13}C_{\mathrm{DIC}}^{\mathrm{mod}} - \delta^{13}C_{\mathrm{DIC}}^{\mathrm{obs}}\right)^2}{\sum \mathrm{vol}\cdot\left(\delta^{13}C_{\mathrm{DIC}}^{\mathrm{obs}} - \left\langle\delta^{13}C_{\mathrm{DIC}}^{\mathrm{obs}}\right\rangle\right)^2} + 0.5\frac{\sum \mathrm{vol}\cdot\left(\mathrm{DIC}^{\mathrm{mod}} - \mathrm{DIC}^{\mathrm{obs}}\right)^2}{\sum \mathrm{vol}\cdot\left(\mathrm{DIC}^{\mathrm{obs}} - \left\langle\mathrm{DIC}^{\mathrm{obs}}\right\rangle\right)^2}, \quad (1)$$

where vol is the volume of the model grid cells and the angle brackets represent the volume-weighted global averages for the tracers. The superscripts mod represents the model and obs represents the observations. While the modeled DIC is taken from a year of 2002 as in the observation (Lauvset et al., 2016), the modeled δ^{13}C are subsampled from the same locations and times as in the observations before calculating the cost function. A formal optimization algorithm based on the unconstrained Nelder-Mead simplex direct search method (Lagarias et al., 1998) is used to find the optimal parameter values that minimize the cost function. Hence, no a priori assumptions nor bounds for the parameter values are imposed in this optimization. The optimization starts from an initial condition of no coastal margin carbon inputs. While simulations are iterated to reach an optimal solution, we save the evolving model input parameter values (chosen by the optimization algorithm) and associated model solutions for uncertainty estimation.

Figure 1. Observed and optimized δ^{13}C in DIC. (a) and (b) Observations (Schmittner et al., 2017) gridded onto model grid cells showing (a) the horizonal distribution at 317 m and (b) the zonally averaged vertical section from the North Atlantic to the Southern Ocean and to the North Pacific. The observation period is 1972–2016. (c) and (d) The simulated δ^{13}C of DIC from the optimized model for the corresponding years to the observations. (e) and (f) The simulated δ^{13}C of DIC from the model that is identical to the optimized model except that coastal margin carbon inputs are set to zero (i.e., terrestrial carbon inputs include only riverine and airborne inputs). (g) and (h) Contribution from the coastal margin carbon input (i.e., the difference between the optimized model and the simulation without the coastal margin carbon input).

Table 1
Input Parameter Values Used for Monte Carlo Simulations and the Comparison With Those for the Standard Model (Red Fonts Indicate Values Obtained From Optimization)

Input parameters	Standard model	Monte Carlo simulations	References
Globally averaged air-sea CO_2 transfer velocity (cm/hr)	15.1 ± 2.5	[14.0 17.0]	(Graven et al., 2012; Naegler et al., 2006; Sweeney et al., 2007; Wanninkhof et al., 2013)
SST for the equilibrium fractionation of $^{13}C/^{12}C$ during air-sea CO_2 exchange	HadISST1	HadISST1	(Rayner et al., 2003)
		ERSSTv5	(Huang et al., 2017)
		COBE-SST2	(Hirahara et al., 2014)
Equilibrium fractionation factors during air-sea CO_2 exchange	$\alpha_{DIC\leftarrow g} = 1.4 \times 10^{-5} \cdot T \cdot f_{CO3} - 1.05 \times 10^{-4} \cdot T + 1.01053$	$\alpha_{DIC\leftarrow g} = 1.4 \times 10^{-5} \cdot T \cdot f_{CO3} - 1.05 \times 10^{-4} \cdot T + (1.01053 \pm 0.00005)$	(Zhang et al., 1995)
Photosynthetic fractionation factors	$\alpha_{OC\leftarrow aq} = -0.00935 \cdot \log_{10}([CO_2]) + 0.99626$	$\alpha_{OC\leftarrow aq} = -0.00935 \cdot \log_{10}([CO_2]) + 0.99626$	(Goericke & Fry, 1994)
		$\alpha_{OC\leftarrow aq} = -0.017 \cdot \log_{10}([CO_2]) + 1.0034$	(Popp et al., 1989)
		$\alpha_{OC\leftarrow aq} = -0.01203 \cdot \log_{10}([CO_2]) + 1.00119$	(Freeman & Hayes, 1992)
The $\delta^{13}C$ values for riverine carbon inputs (‰)	DOC: −27	DOC: −27 ± 2	(Marwick et al., 2015; Peterson & Fry, 1987)
	POC: −30	POC: −30 ± 2	
	DIC: −15	DIC: −15 ± 2	
Sedimentary burial of inorganic carbon (GtC/yr)	0.2 ± 0.1	[0.1 0.3][a]	(Milliman, 1993; Sarmiento & Sundquist, 1992)
Preindustrial $\delta^{13}C$ value for atmospheric CO_2 (‰)	−6.5	[−6.5 −6.3][b]	(Rubino et al., 2013)
Ocean circulation model[c]	$\omega 2$	CTL, $\omega 2$, $\omega 4$, $K_{I,\,2000}$, $K_{I,600}$, $K_{V,1.5}$, $\gamma_{0.27}$, P1, P2, P3	(DeVries, 2014)

[a]Because our model assumes a steady-state during the preindustrial era, the inorganic carbon burial implemented in the model is a portion that is balanced by terrestrial carbon inputs. Therefore, the previously reported range of 0.2–0.4 GtC/yr is adjusted to a balanced sink of 0.1–0.3 GtC/yr. [b]The range is bracketed by a preindustrial mean value and a value as of 1780, both of which are constrained by Rubino et al. (2013). [c]The suite of ocean circulation models have slightly different temperature and salinity as well as different ocean mixing, leading to different surface productivity and carbonate chemistry in seawater.

3.4. Uncertainty Estimation

We provide error estimates based on both the results of the optimization experiment, and based on a more comprehensive assessment of the uncertainty in a series of Monte Carlo simulations. Optimization-based uncertainties are calculated from the set of model solutions within the parameter space explored by the optimization that results in a 1% increase in the value of the cost function (Equation 1). This is a somewhat ad-hoc measure of uncertainty that tells how well-defined the cost function minimum is for the parameter space explored during the optimization procedure. We also attempt a more formal uncertainty estimate using a series of Monte Carlo simulations to explore the influence of various model assumptions and parameters on our results. These experiments address uncertainties in the preindustrial $\delta^{13}C$ value for atmospheric CO_2, the equilibrium fractionation factors for air-sea CO_2 exchange, the $\delta^{13}C$ values of riverine carbon inputs, the air-sea CO_2 exchange rate, the sea surface temperature used in the calculation of air-sea CO_2 exchange, the photosynthetic fractionation factor for $\delta^{13}C$, the ocean circulation model, and the carbon burial rate (Table 1; Section 5.2). We also perform sensitivity experiments to assess the effect of varying the isotopic composition and lability of the coastal margin carbon inputs (Section 5.3). We also address uncertainties related to the representation of carbon burial, the isotopic composition of riverine carbon, the formulation of air-sea CO_2 gas exchange, and the representation of industrial changes in coastal margin inputs (Section 5.4; Text S2).

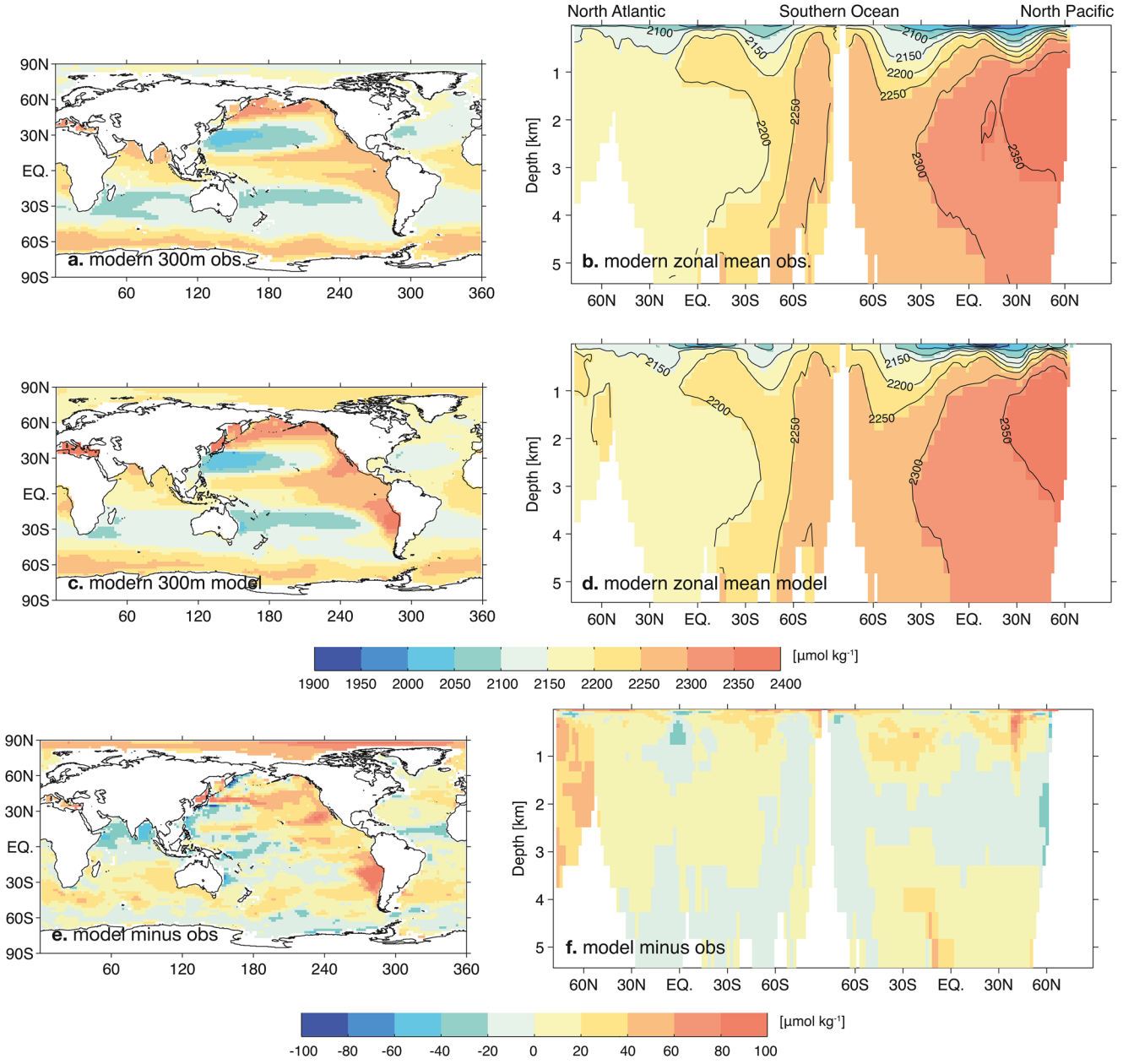

Figure 2. Observed and simulated $DI^{12}C$ from the optimized model. (a) and (b) Observations (Lauvset et al., 2016) gridded onto model grid cells showing (a) the horizontal distribution at 317 m and (b) the zonally averaged vertical section from the North Atlantic to the Southern Ocean and to the North Pacific. The observation is referenced to 2002. (c) and (d) DIC simulated from the optimized model as of 2002. (e) and (f) Differences between the model and observations, that is, (c) minus (a) is shown in (e), and (d) minus (b) is shown in (f).

4. Carbon Fluxes in the Optimized Model

4.1. Overview of Results from the Optimized Model

Optimizing the parameters of our model (Figures 1 and 2) yields a globally integrated terrestrial carbon input to the ocean of 1.4 ± 0.2 GtC/yr for the preindustrial and industrial era, where the uncertainty is based on the cost function criterion defined in Section 3.4. The terrestrial carbon source of 1.4 ± 0.2 GtC/yr exceeds the prescribed riverine carbon inputs of 0.61 GtC/yr (Mayorga et al., 2010; Meybeck & Ragu, 2012), as well as previous estimates of the total terrestrial carbon input to the ocean which average around 0.9 GtC/yr (Cole et al., 2007). The estimated coastal margin carbon input of 0.8 ± 0.2 GtC/yr (the difference between

total carbon inputs and prescribed riverine inputs) is also higher than estimates based on meteoric groundwater fluxes and uncertainties in the prescribed riverine carbon inputs (Raymond, 2007), which together may account for up to 0.4 GtC/yr (Cole et al., 2007). The excess is likely driven by lateral export of carbon from estuaries, mangroves, salt marshes, and intertidal freshwater forests (Abril et al., 2013; Alongi & Mukhopadhyay, 2014; Bauer et al., 2013; Chen et al., 2018; Cole et al., 2007; Maher et al., 2013; Moore, 2010; Rosentreter et al., 2018; Szymczycha et al., 2014). In fact, the optimized $\delta^{13}C$ value for the coastal margin input of $-(26 \pm 5)$‰ falls within the observed $\delta^{13}C$ of groundwater-driven carbon fluxes from coastal wetlands, which span $-(14–30)$‰ (Abril et al., 2013; Maher et al., 2013). These ^{13}C-depleted coastal margin inputs are necessary to match the observed $\delta^{13}C$ of DIC, which in the model would be 0.2‰–0.3‰ higher than observed throughout the global ocean without the coastal margin input (Figures 1g and 1f; see also the discussion in Section 5.1).

Although our result is based only on achieving maximal consistency with observed oceanic DIC and the subsurface $\delta^{13}C$ in DIC, the model solution is also consistent with other independent observational constraints. The model matches with observation-based estimates for the isotopic disequilibrium of CO_2 (Figure 3; see Section 4.2) and for open-ocean air-sea CO_2 fluxes (Figure 4; see Section 4.3). The model also captures the anthropogenic perturbations in the oceanic storage of anthropogenic carbon and in the surface-averaged $\delta^{13}C$ of DIC (Figure 5). The optimization results in a globally averaged air-sea CO_2 transfer velocity of 15.1 ± 2.5 cm/hr, which compares well with previous estimates of 14–17 cm/hr (Sweeney et al., 2007; Wanninkhof et al., 2013), and a globally integrated sedimentary carbonate burial flux of 0.22 ± 0.06 GtC/yr, which is within the range of 0.2–0.4 GtC/yr from previous estimates (Milliman, 1993; Sarmiento & Sundquist, 1992). Our optimal model also infers negligible anthropogenic perturbations in terrestrial carbon inputs within the uncertainty range of ±0.2 GtC/yr, and also negligible anthropogenic perturbations in the $\delta^{13}C$ value of the coastal margin input within ±5‰ (see a further discussion in Text S2). These results are in accord with previous analyses suggesting that opposing effects from climate change, land use change, dam constructions, and sea level rise have resulted in net near-zero perturbations to terrestrial carbon fluxes on a global scale (Duarte, 2017; Moore, 2010; Regnier et al., 2013). The overall consistency of our results with all of these independent constraints provides support for the realism of the model.

4.2. The Isotopic Disequilibrium of CO_2

The isotopic disequilibrium of gaseous CO_2 is an important constraint on the oceanic carbon isotope budget (Quay et al., 2003; Sonnerup & Quay, 2012; Tans et al., 1993). The isotopic disequilibrium of CO_2 is defined as the difference between the observed $\delta^{13}C$ of atmospheric CO_2 and the $\delta^{13}C$ value that the atmospheric CO_2 would have if the atmosphere were in equilibrium with the surface ocean (Gruber & Keeling, 2001; Quay et al., 2003). This isotopic disequilibrium of CO_2 can be computed as "$\delta^{13}C$ disequilibrium = $\delta^{13}C$ in surface DIC - (ε_{DIC-g})- $\delta^{13}C$ in atmospheric CO_2" where (ε_{DIC-g}) is the fractionation factor from gaseous CO_2 to DIC in ‰ (Quay et al., 2017). During the preindustrial era, ^{13}C-depleted terrestrial carbon inputs to the ocean were balanced with ^{13}C-enrichments at the sea surface, which set the isotopic disequilibrium of CO_2 (the $\delta^{13}C$ disequilibrium hereinafter). During the industrial era, the $\delta^{13}C$ disequilibrium has increased because the ^{13}C-depletion in the atmospheric CO_2 has outpaced the ^{13}C-depletion in the oceanic surface DIC. Since the surface $\delta^{13}C$ of DIC is not used as a constraint for the optimization (Section 3.2), the fidelity of our model results can be tested by comparing the simulated $\delta^{13}C$ disequilibrium to previous observation-based estimates.

Our estimate for the globally averaged $\delta^{13}C$ disequilibrium with area-weighting is 0.86 ± 0.06‰ as of 1995, which compares well with a previous estimate of 0.88 ± 0.1‰ (Quay et al., 2003) and an estimate using the global database of 0.88‰ (Schmittner et al., 2017) (Figure 3e). The comparison between the model and previous estimates becomes more challenging when we compare the globally averaged $\delta^{13}C$ disequilibrium weighted by gross CO_2 fluxes. Indeed, previous studies suggested globally averaged $\delta^{13}C$ disequilibrium values ranging from 0.43‰ (Tans et al., 1993) to 0.60 ± 0.1‰ (Quay et al., 2003), and as high as 0.75 ± 0.1‰ (Quay et al., 2017), where the latter two estimates are referenced to the same time period of the 1990s. The large spread partly stems from the sensitivity of the estimate to the formulations of air-sea CO_2 transfer rates and wind speed data used for the estimates. Using our optimized gross CO_2 fluxes, our estimate of 0.79 ± 0.06‰ as of 1995 agrees with the latest estimate of 0.75 ± 0.1‰ for the 1990s (Quay et al., 2017).

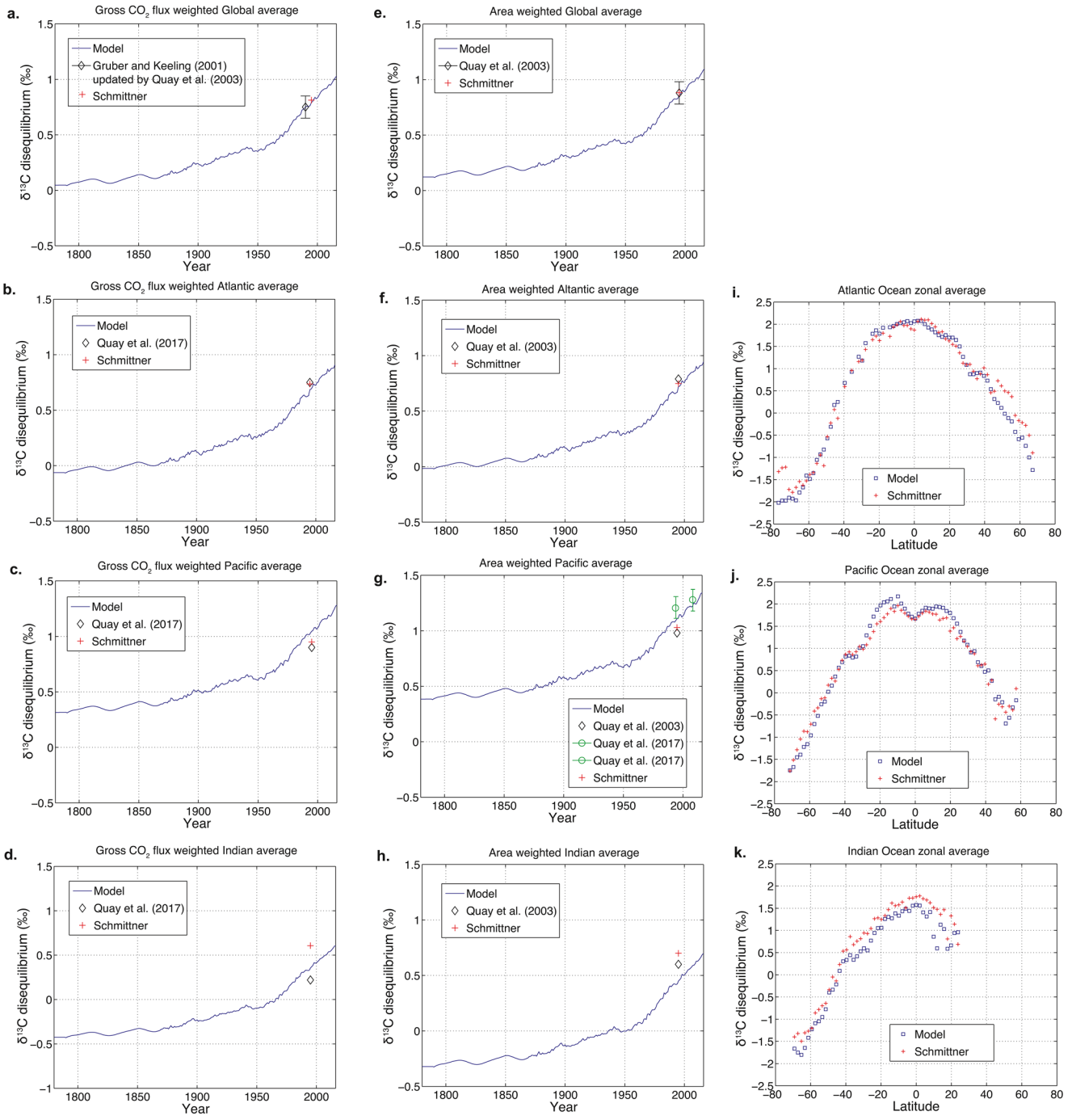

Figure 3. The $\delta^{13}C$ disequilibrium ($\delta^{13}C$ disequilibrium = $\delta^{13}C$ in surface DIC - (ε_{DIC-g})- $\delta^{13}C$ in atmospheric CO_2 where (ε_{DIC-g}) is the fractionation factor from gaseous CO_2 to DIC in ‰) estimated from the optimized model and observations. (a) The global averages weighted by gross air-to-sea CO_2 fluxes. The model estimate (blue line) is compared with an estimate from Gruber and Keeling (2001) and Quay et al. (2003) (black diamond) and an estimate based on the observations (Schmittner et al., 2017) (red cross). (b)–(d) The gross CO_2 flux-weighted averages for the Atlantic, Pacific, and Indian Oceans. (e) The global averages weighted by area. (f)–(h) The area-weighted averages for the Atlantic, Pacific, and Indian Oceans. (i)–(k) The zonally averaged air-sea $\delta^{13}C$ disequilibrium for the Atlantic, Pacific, and Indian Oceans. The model estimates (blue squares) are compared with the estimates based on the observations (Schmittner et al., 2017) (red crosses). The global and basin-scale averages are made by subsampling the model at the locations where the observations (Schmittner et al., 2017) are available.

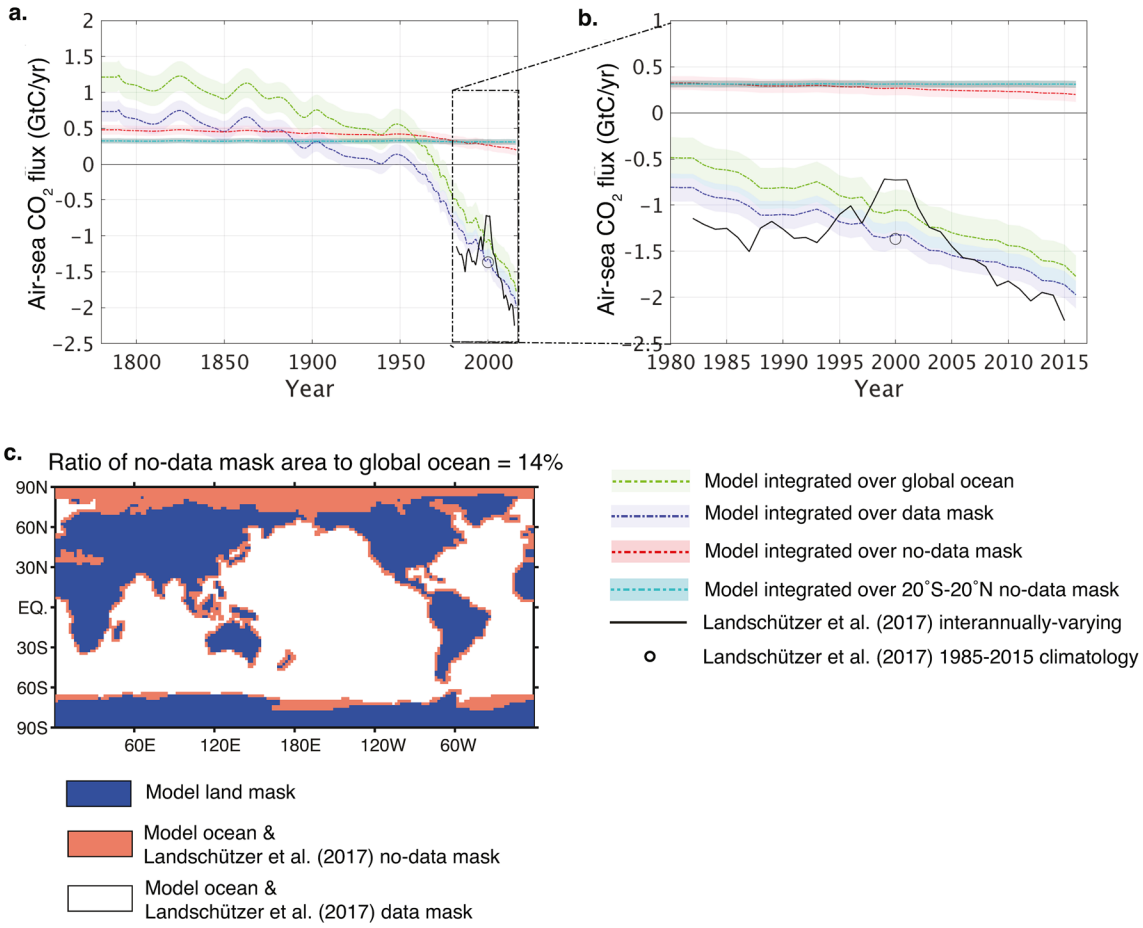

Figure 4. Air-sea CO_2 fluxes. (a) Globally integrated air-sea CO_2 flux from the optimized model (green dashed line) is divided into the flux integrated over the data mask (blue dashed line) and the no-data mask (red dashed line). The black solid line shows the interannually varying estimate (Landschützer et al., 2017) based on oceanic pCO_2 observations from 1982 to 2015 and the black circle shows the 1985–2015 climatological-mean value of the Landschützer et al. (2017) data set. The cyan dashed line shows the flux integrated over the no-data mask between 20°S and 20°N. Negative fluxes represent a CO_2 uptake by the ocean while positive fluxes represent an outgassing to the atmosphere. The uncertainty shown in the color shading is equivalent to a 1% increase in the cost function value. (b) The plot from 1980 to 2016 in (a) is zoomed in. (c) The data (white) and no-data (red) masks used for the spatial integration in (a) and (b).

Furthermore, our model-based estimate of 0.75 ± 0.06‰ as of 1990 also matches precisely with an estimate of 0.75 ± 0.1‰, a value estimated by Quay et al. (2003) by reassessing results of Gruber and Keeling (2001) with an updated $\delta^{13}C$ value of atmospheric CO_2 (Figure 3a). The consistencies in the globally averaged $\delta^{13}C$ disequilibrium between this study and the independent observation-based estimates provides strong support for the results of the optimized model.

In addition to the agreement at the global scale, the optimized model also captures the general latitudinal patterns of the $\delta^{13}C$ disequilibrium estimated using the global database (Schmittner et al., 2017) (Figures 3i–3k) and those estimated in previous studies (Gruber & Keeling, 2001; Quay et al., 2003, 2017). There is a slight tendency for the model to overestimate $\delta^{13}C$ disequilibrium in the low latitudes and underestimate it in the high latitudes, which could be due to the lack of seasonality in the model. Nonetheless, when the simulated $\delta^{13}C$ disequilibrium is globally averaged with area-weighting or gross-flux-weighting, these small latitudinal biases are offset (Figures 3a and 3e). Thus, there is no indication of any systematic global bias arising from the lack of seasonality in the model.

4.3. Air-Sea CO_2 Exchange in the Open Ocean

The 1.2 ± 0.2 GtC/yr outgassing of natural CO_2 estimated in the optimized model implies a net oceanic uptake of atmospheric CO_2 of 1.1 ± 0.2 GtC/yr as of 2000, given our estimated anthropogenic CO_2 uptake of

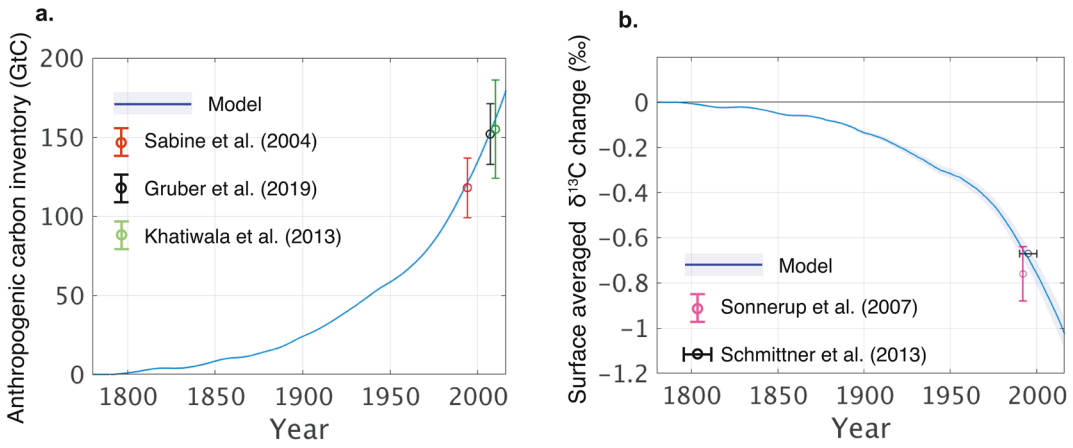

Figure 5. Oceanic storage of anthropogenic carbon and globally averaged δ^{13}C-DIC at the sea-surface simulated from the optimized model. (a) Cumulative storage of anthropogenic carbon simulated by the model (blue line) is compared with the estimates by Sabine et al. (2004) (red), Gruber et al. (2019) (black), and Khatiwala et al. (2013) (green). (b) Anthropogenic change in globally averaged surface δ^{13}C-DIC simulated by the model (blue line) is compared with the estimates by Schmittner et al. (2013) (black circle) and Sonnerup et al. (2007) (magenta). The blue shading around the blue line is equivalent to a 1% increase in the cost function value.

2.3 GtC/yr (Figure 4). This global oceanic CO_2 uptake is below previous estimates derived from the observed oceanic pCO_2 (1.4 ± 0.5 GtC/yr as of 2000) (Landschützer et al., 2017) and ocean inverse models (1.7 ± 0.4 GtC/yr as of 1995–2000) (Gruber et al., 2009). The discrepancy would be even larger if we compare our estimates with Watson et al. (2020) who suggested an upward revision of a previous estimate of 1.4 ± 0.5 GtC/yr by 0.8–0.9 GtC/yr. Much of this difference can be attributed to the fact that the global integrations were made over different spatial areas. To demonstrate this, we compare the air-sea CO_2 fluxes from our optimal model to that from a pCO_2-based reconstruction of oceanic CO_2 uptake (Landschützer et al., 2017) over the ocean area covered by the pCO_2-based product. For this comparison, we linearly interpolated the 1° × 1° data mask from Landschützer et al. (2017) to our 2° × 2° model grid cells (Figure 4c). We refer to the interpolated data mask as the "open ocean" mask, whereas the remaining ocean grid cells are referred to as the "coastal ocean" mask (which includes coastal margins and most of the Arctic Ocean). Over the open ocean, a preindustrial efflux of 0.7 ± 0.2 GtC/yr is superimposed by an anthropogenic CO_2 uptake of 2.1 GtC/yr to yield a net uptake of 1.4 ± 0.2 GtC/yr as of 2000. This agrees well with the pCO_2-based estimate of a 1.4 ± 0.5 GtC/yr uptake averaged over 1985–2015 (Landschützer et al., 2017) (Figure 4b). Our open-ocean estimate of the preindustrial CO_2 outgassing (0.7 ± 0.2 GtC/yr) also agrees with an estimated efflux of 0.78 GtC/yr that is consistent with interhemispheric ocean heat and carbon transports (Resplandy et al., 2018).

This agreement between the air-sea fluxes in the optimized model and those from independent estimates occurs despite the lack of seasonal cycle in the model, which leads to winter-like surface properties (e.g., DIC and SST) at the sea surface where deep and intermediate waters form and subduct (DeVries & Primeau, 2011; DeVries, 2014). These winter-like surface properties accompany outgassing-favorable pCO_2 and air-sea CO_2 fluxes in upwelling regions, and opposing uptake-favorable pCO_2 and air-sea CO_2 fluxes in the high-latitude North Atlantic and mid-latitude surface regions where winter cooling leads to CO_2 uptake (Figure S3). When globally integrated or averaged, these opposing spatial biases largely offset, resulting in a net air-sea CO_2 flux similar to the ones obtained either from observations or seasonally resolved models (Figure 4). As a further indication that the lack of seasonality is not biasing the ocean ventilation and CO_2 uptake, the simulated oceanic uptake of anthropogenic CO_2 in the optimized model agrees well with previous observation-based estimates (DeVries, 2014; Gruber et al., 2019; Khatiwala et al., 2013; Sabine et al., 2004) (Figure 5).

4.4. Air-Sea CO_2 Exchange in the Coastal Ocean

The only area where the optimal model does not agree well with independent observational constraints is in the “coastal ocean” (Figure 4c). Over this region, CO_2 efflux has weakened from 0.5 ± 0.1 GtC/yr during

preindustrial times to 0.3 ± 0.1 GtC/yr as of 2000 (Figure 4a). Our estimate for the 2000s is within the uncertainty range of an earlier estimate of a 0.06 ± 0.43 GtC/yr efflux (Laruelle et al., 2010), but contrasts with a 0.04 ± 0.05 GtC/yr uptake recently proposed for the global coastal regions, which include continental shelves and estuaries (Laruelle et al., 2013, 2014) (Figure S2b). The discrepancy becomes even larger if we compare our estimate with a 0.3 GtC/yr uptake suggested by Chen et al. (2013). A number of factors could contribute to the discrepancy between our optimal model and the observation-based estimates. Applying a different geographical definition for the coastal regions using the criterion of isobaths less than 1,000 m or distance from the coastline less than 300 km (which was proposed by Laruelle et al. (2017) in order to facilitate integration of coastal observations to global models), our model suggests a 0.2 ± 0.1 GtC/yr outgassing of CO_2 as of 2000 (Figure S2b). The use of the Laruelle et al. (2017) definition thus narrows the gap with the observation-based estimates but still implies a larger CO_2 efflux than previously estimated. An additional factor is the potential for increased productivity in coastal regions due to anthropogenic nutrient supplies (Laruelle et al., 2018; Mackenzie et al., 2011). An idealized experiment using our model suggests that an increased nutrient supply that leads to a 2% increase in the coastal surface PO_4 concentrations could reduce the coastal CO_2 efflux by 0.1 GtC/yr as of 2000, by exporting organic carbon to the open ocean (Figures S2d and S2e).

It is also possible that previous studies might have underestimated a low-latitude coastal CO_2 efflux due to insufficient observations (Laruelle et al., 2013, 2014, 2017). In fact, our model shows that the poorly monitored low-latitude coastal regions between 20°S and 20°N account for 70% of the total coastal efflux in a year of 1800 and 100% in a year of 2000 (Figure 4a). These low-latitude coastal regions are known to have low CO_2 solubility and monsoon-driven upwelling (Cai, 2011; Laruelle et al., 2014, 2017). Moreover, these regions are densely populated by mangrove forests, which globally export 0.1–0.4 GtC/yr to the intertidal and coastal zones (Alongi & Mukhopadhyay, 2014; Chen et al., 2018; Rosentreter et al., 2018), supporting the potential need for an elevated outgassing of CO_2 from surrounding seawater. Although a persistent outgassing of as much as 0.3 GtC/yr from the low-latitude (20°S-20°N) coastal regions remains to be confirmed or disproved by future observational studies, the low-latitude dominance in the coastal CO_2 efflux is qualitatively consistent with previous studies (Cai, 2011; Laruelle et al., 2014, 2017). The reduced CO_2 efflux from 0.5 GtC/yr in 1780 to 0.3 GtC/yr in 2000, and hence the estimated anthropogenic CO_2 uptake of 0.2 GtC/yr over the coastal domain is consistent with a previous observation-based estimate of 0.17 GtC/yr (Borges, 2005), but is larger than a model-based estimate of 0.10 ± 0.01 GtC/yr for 1994–2012 (Bourgeois et al., 2016).

Imperfections in the model could also contribute to some of the discrepancies between our coastal ocean CO_2 budget and that of previous studies. Our coarse-resolution model does not resolve the small-scale spatial gradients in the coastal region, nor does it realistically represent the connectivity between the coastal regions and the open ocean. Given the long air-sea equilibration time of $\delta^{13}C\text{-}CO_2$ compared to $^{12}CO_2$, a portion of the terrestrial carbon inputs that are inferred here as necessary to balance the open-ocean $\delta^{13}C$ budget could be balanced by CO_2 outgassing further upstream along the land-ocean continuum, such as in estuaries and tidal wetlands. Furthermore, our model does not resolve all of the sedimentary burial of organic and inorganic carbon in shelves and estuaries, which could help to balance some of the carbon that is currently estimated to outgas in this region. These issues of scale preclude a perfect comparison between our results and those of previous studies, and point toward the need to better resolve coastal processes in the model in order to better constrain coastal ocean CO_2 fluxes.

4.5. Basin-Scale Distribution of Terrestrial Carbon Inputs

In the standard model, the coastal margin carbon fluxes are distributed uniformly across all continental margins, except for Antarctica. Although this is an obvious oversimplification of the spatial distribution of coastal margin carbon inputs, oceanic observations of carbon isotopes cannot be used to constrain the regional distributions of land-sourced carbon fluxes. This is because ocean circulation integrates and smooths the effects of regional sources and sinks, producing large-scale spatial gradients on the ocean basin to global scale. Hence, we here use our model to explore interbasin contrasts in coastal margin carbon inputs. To do so, we separately optimize the coastal margin carbon fluxes for the Arctic-Atlantic, Pacific, and Indian Oceans (the "Basin" experiment in Table S1; see Text S1), along with the other model

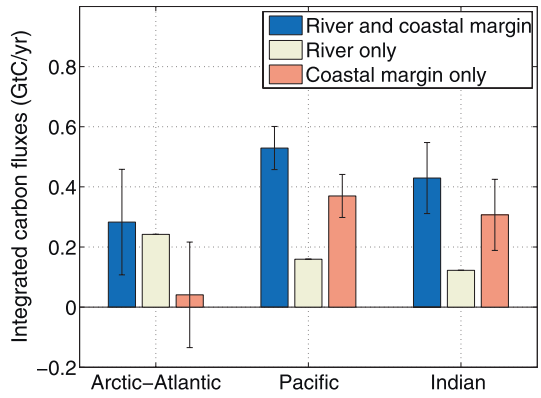

Figure 6. Terrestrial carbon fluxes divided into three ocean basins (results from the "Basin" experiment). The sum of riverine and coastal margin carbon fluxes is integrated over the Arctic-Atlantic, Pacific, and Indian Ocean (blue bar). The sum is divided into the contribution from rivers (yellow bar) and from coastal margin fluxes (red bar). The uncertainty is equivalent to a 1% increase in the unexplained variance of the observed DIC and the $\delta^{13}C$ of DIC, and takes into account intercorrelated errors among ocean basins.

parameters. This model also yields a globally integrated coastal margin input of 0.8 ± 0.1 GtC/yr. This model further suggests that most of the coastal margin carbon inputs occur in the Pacific (52 ± 9%) and Indian Oceans (43 ± 16%) where the basin-integrated total carbon fluxes exceed the prescribed riverine fluxes by a factor of 3.3 ± 0.4 in the Pacific, and 3.5 ± 0.9 in the Indian Ocean (Figure 6). Combined with the prescribed riverine carbon input, the Pacific and Indian Oceans contribute to 77 ± 6% of the terrestrial carbon inputs to the global ocean. The dominance of coastal margin carbon fluxes in the Pacific and Indian Oceans is consistent with these basins having the largest spatial extent of coastal vegetation (Chen et al., 2018), and coincides with regions that have the lowest density of coastal pCO_2 observations (Laruelle et al., 2017). In contrast, riverine fluxes dominate the total carbon flux in the Arctic-Atlantic, accounting for 86 ± 33% of the total terrestrial carbon flux. This basin-wide contrast in coastal margin carbon inputs is similar to the basin-scale distribution of SGD-driven ^{228}Ra fluxes, which is also dominated by the Indian and Pacific Ocean (Kwon et al., 2014). This makes sense, since the recirculation of seawater through coastal aquifers may result in enhanced discharge of Ra as well as terrestrial carbon into the coastal ocean.

5. Model Uncertainties and Impact on Estimated Carbon Fluxes

The optimized model provides an estimate of terrestrial carbon fluxes to the ocean that is optimally consistent with the observed $\delta^{13}C$-DIC and DIC distributions in the ocean, and with numerous independent constraints on the open ocean air-sea CO_2 fluxes and the air-sea $\delta^{13}C$ disequilibrium fluxes (Section 4). However, the values of the terrestrial carbon flux found in this simulation may also be influenced by other assumptions and/or limitations in the model. Here, we explore some of these assumptions and limitations, in an attempt to gauge how well constrained the terrestrial carbon fluxes are in our model. First, we explore whether the model parameters could be adjusted such that additional coastal margin carbon inputs are not needed in order to match the observed carbon isotope constraints (Section 5.1). Then, we perform a series of Monte Carlo experiments to characterize the uncertainty arising from a realistic range of parameters and assumptions in the model (Section 5.2). Finally, we explore how our model results vary if we consider additional uncertainties in the lability and isotopic composition of coastal margin carbon inputs to the ocean (Section 5.3). We summarize the overall uncertainty assessments in Section 5.4.

5.1. Assessing Models With and Without Coastal Margin Carbon Inputs

We first explore whether there are any parameter combinations in the model that could yield a match between the modeled and observed oceanic carbon isotope composition, in the absence of coastal margin carbon inputs. For this, we vary the parameters and input data of our model within a wide range of plausible values, and run the model both with and without the coastal margin carbon inputs. For the simulations with coastal margin carbon inputs, we fix the magnitude and isotopic composition of the coastal margin source at the value obtained from the optimized model (0.8 GtC/yr and −26‰, respectively). Parameters and inputs of the model that are varied in these experiments include the preindustrial $\delta^{13}C$ value for atmospheric CO_2, the equilibrium fractionation factors for air-sea CO_2 exchange, the $\delta^{13}C$ values of riverine carbon inputs, the air-sea CO_2 exchange rate, the SST used for carbon isotope fractionation, the photosynthetic fractionation factors, the ocean circulation model, and the portion of terrestrial carbon inputs that is buried in marine sediments (see Table 1 for summary and references). For each simulation, we randomly select parameter values and model configurations from the ranges listed in Table 1, assuming they are uniformly distributed within their upper and lower bounds, and solve the model with the selected combination of parameters. We repeat this 800 times for each model (with and without coastal margin carbon inputs). We then compare the simulated to the observed mean ocean subsurface $\delta^{13}C$-DIC, and the global mean area- and flux-weighted air-sea $\delta^{13}C$ disequilibrium.

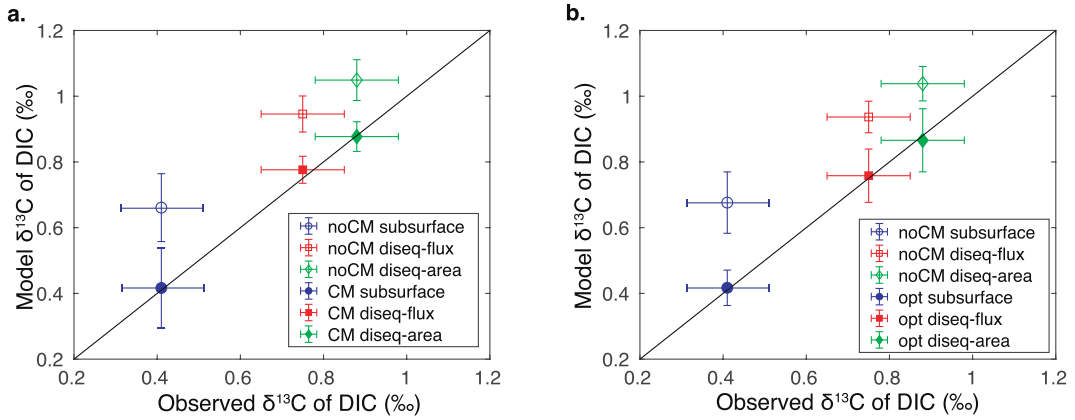

Figure 7. Model-observation comparison of $\delta^{13}C$ in DIC. The model values in *Y*-axis are compared with the respective observation-based estimates in *X*-axes. Open symbols ("noCM") show the median values from the Monte Carlo experiment based on the model without the coastal margin input, and the error bars represent 95% confidence intervals from the Monte Carlo simulation. (a) Filled symbols ("CM") show the median values from the Monte Carlo experiment based on the model with the coastal margin input, and the error bars represent 95% confidence intervals from the Monte Carlo simulation. Blue symbols show the globally averaged subsurface $\delta^{13}C$-DIC ("subsurface"), using an observational constraint from Schmittner et al. (2017) with an error bar of ±0.1‰. Red symbols show the globally averaged air-sea $\delta^{13}C$ disequilibrium as of 1990 estimated with gross CO_2 flux-weighting ("diseq-flux"), using observational constraints from Gruber and Keeling (2001) and Quay et al. (2003). Green symbols show the globally averaged $\delta^{13}C$ disequilibrium as of 1995 calculated with area-weighting ("diseq-area"), using an observational constraint from Quay et al. (2003). (b) The same as (a) except that the filled symbols ("opt") show the values from the optimized model with error bars determined based on a 1% increase in cost function value.

We find that the model with coastal margin inputs is consistent with the $\delta^{13}C$-DIC observational constraints even when these various aspects of model uncertainty are collectively considered (Figure 7a). The modeled subsurface $\delta^{13}C$ of DIC is 0.43 ± 0.1‰, almost exactly matching the observed value of 0.41 ± 0.1‰ (Schmittner et al., 2017). The area-weighted and flux-weighted DIC disequilibrium are 0.87 ± 0.04‰ as of 1995 and 0.77 ± 0.04‰ as of 1990, respectively, almost exactly matching the observed values of 0.88 ± 0.1‰ (Quay et al., 2003) and 0.75 ± 0.1‰ (Gruber & Keeling, 2001; Quay et al., 2003) (Figure 7a). For comparison, the values derived from the optimized model have a similar mean and uncertainty (based on the cost function criterion) as the Monte Carlo experiments with the coastal margin carbon inputs (Figure 7b). On the other hand, the model without coastal margin carbon inputs exhibits a globally averaged subsurface $\delta^{13}C$-DIC and air-sea $\delta^{13}C$ disequilibrium that are both 0.2‰–0.3‰ higher than observed (Figure 7). This systematic and globally distributed 0.2‰–0.3‰ offset exceeds the observational uncertainty of ~0.1‰, and exceeds the 95% confidence intervals derived from the Monte Carlo experiments (Figure 7a). The magnitude of the offset is quite large given the spatial variations of the observed $\delta^{13}C$-DIC, which have a standard deviation of 0.45‰ and a full range of −1‰ to 2‰ (Figure 1). Overall, these Monte Carlo simulations demonstrate that any combinations of the model parameters and inputs shown in Table 1 cannot produce $\delta^{13}C$ values that match the observations within their uncertainties, without requiring additional $\delta^{13}C$-depleted coastal margin carbon inputs.

5.2. Assessing the Uncertainty of the Coastal Margin Carbon Source

The Monte Carlo experiments above (Figure 7) clearly demonstrate that some amount of coastal margin carbon inputs is necessary in our model in order to match the observed mean-ocean $\delta^{13}C$-DIC and air-sea $\delta^{13}C$ disequilibrium. In order to better assess the uncertainty of the magnitude of coastal margin carbon inputs required in the model, we performed another set of Monte Carlo experiments like in Section 5.1, again randomly selecting parameters and model configurations from the list in Table 1, but this time also allowing the coastal margin carbon input to vary between 0 and 1.4 GtC/yr (a random selection assuming a uniform distribution). From 1000 ensemble members, we select those that match the observational constraints shown in Figure 7 (the global mean subsurface $\delta^{13}C$ and air-sea $\delta^{13}C$ disequilibrium) within their uncertainty, while also ensuring that the resulting simulations reasonably capture the observed $\delta^{13}C$-DIC and

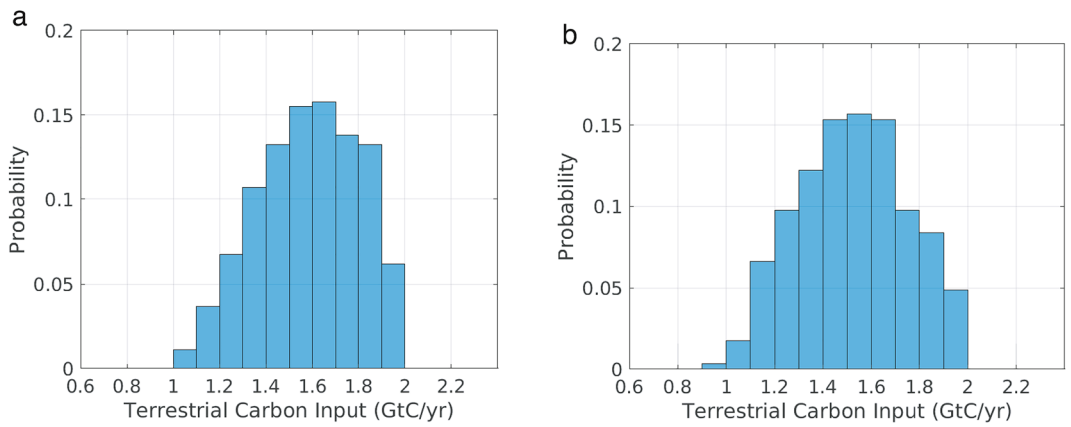

Figure 8. The probability distribution of the terrestrial carbon inputs to the global ocean in a series of model configurations that fit the observed carbon isotope constraints within their uncertainty (a) The probability distribution of terrestrial carbon inputs from a set of Monte Carlo experiments where the coastal margin input (assuming a uniform distribution between 0 and 1.4 GtC/yr) and the other model parameters in Table 1 are randomly selected. Note that the terrestrial carbon input on the *X*-axis is the sum of the prescribed riverine and aerosol-driven input of 0.6 GtC/yr, and the additional coastal margin input. (b) The probability distribution in (a) is modified by incorporating the uncertainties arising from the $\delta^{13}C$ value of the coastal margin input (assuming a uniform distribution between −16‰ and –36‰) and the e-folding lifetime (assuming a uniform distribution within 0–20 years) for the half of the coastal margin input.

DIC by selecting models that do not exceed the RMSEs of the optimized model by 0.1‰ and 10 μmol/kg, respectively. Three hundred twenty-nine out of the 1,000 ensemble members meet these criteria. The probability distribution of terrestrial carbon inputs in this selection of models is shown in Figure 8a, which shows that a terrestrial carbon flux as low as 1.0 GtC/yr (a coastal margin carbon source of 0.4 GtC/yr) could be consistent with the observed $\delta^{13}C$-DIC and air-sea $\delta^{13}C$ disequilibrium. Overall, this set of simulations has a highest probability in a terrestrial carbon source of 1.6 GtC/yr, falling within the upper bound of our optimized value of 1.4 ± 0.2 GtC/yr.

5.3. Additional Uncertainties due to the Isotopic Composition and Lability of Terrestrial Carbon

The Monte Carlo simulations (Figure 8a) still potentially miss some important sources of uncertainty that could affect the inferred coastal margin carbon input. Two of the most important of these are the $\delta^{13}C$ signature of coastal margin carbon inputs, which is fixed at a value of −26‰ from the optimized model, and the lability of this coastal margin carbon source, which is assumed to be in a form of DIC or easily degradable organic carbon. Observations suggest that the $\delta^{13}C$ of carbon derived from SGD or coastal vegetation could range from −10‰ to −34‰ (Abril et al., 2013; Maher et al., 2013; Marwick et al., 2015; Peterson & Fry, 1987), while the lability of terrestrial organic carbon varies over a wide spectrum with lifetimes spanning from days to centuries for various fractions (Anderson et al., 2019; Polimene et al., 2018; Raymond, 2007). Any misspecification of these parameters can propagate to errors in the magnitude of the coastal margin carbon inputs.

To explore the sensitivity of our model to these parameters and assumptions, we simultaneously vary the $\delta^{13}C$ of coastal margin carbon inputs, the magnitude of coastal margin carbon inputs, and the e-folding lifetime of the coastal margin carbon inputs. Other model parameters are fixed at those determined in the optimized model, except that the e-folding lifetime of riverine DOC is assumed to be 2 years (Anderson et al., 2019) instead of 8 years. We vary the $\delta^{13}C$ of the coastal margin carbon source from −1‰ to −41‰, encompassing the observed range, and we vary the coastal margin carbon input from 0 to 2.0 GtC/yr. For the lability of coastal margin carbon inputs, we assume that a half of the coastal margin carbon inputs are in organic form with a lifetime ranging from 0 to 50 years, while the other half is in the form of DIC (e.g., Maher et al. (2018)). The results show that a broad range of coastal margin carbon inputs could be reasonably consistent with the observed $\delta^{13}C$-DIC and DIC distributions (Figures 9a and 9b). The coastal margin $\delta^{13}C$ values within the range of roughly −20‰ to −40‰ could be consistent with the coastal margin carbon inputs ranging from 0.4 to 1.2 GtC/yr (Figure 9a), whose upper bound appears to be better constrained by

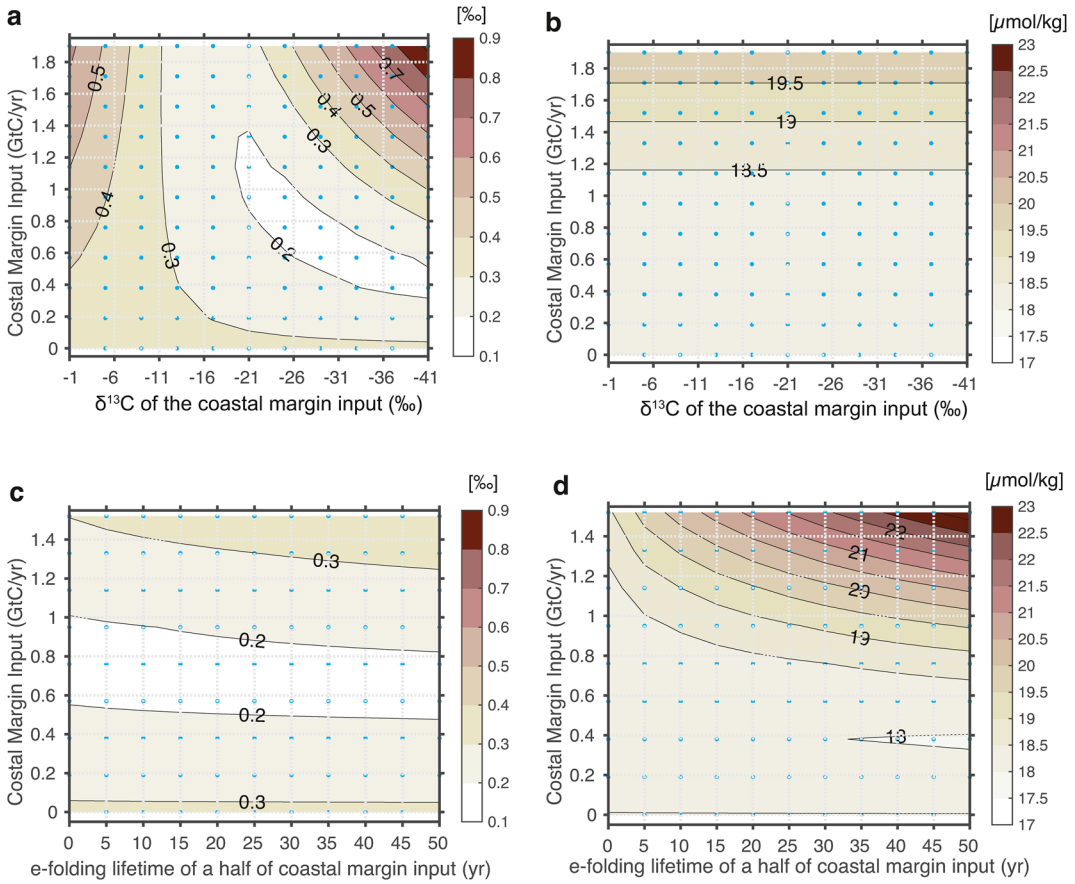

Figure 9. Sensitivity of model-observation misfits to model parameters. (a) The sensitivity of the RMSE for δ^{13}C-DIC to the magnitude and δ^{13}C value of the coastal margin input. The other model parameters are all fixed at those from the optimized model. The results from model simulations are marked as blue dots whereas the contours and shading are based on interpolations. (b) Same as (a) except that the RMSE for DIC is shown. (c) The sensitivity of the RMSE for δ^{13}C-DIC to the coastal margin input and the e-folding lifetime (representing the lability of DOC) of half of the coastal margin carbon input. The other model parameters are all fixed at those from the optimized model except that the e-folding lifetime of riverine DOC is prescribed at 2 years instead of 8 years. (d) Same as (c) except that the RMSE for DIC is shown.

observed DIC than δ^{13}C-DIC. Changing the lifetime of the coastal margin carbon inputs does not have as large an effect on the inferred coastal margin carbon source, but the results do demonstrate that a potential underestimation of the lifetime (an overestimation of the lability) of the coastal margin inputs would lead to an overestimation of the coastal margin input. Very long lifetimes of coastal margin carbon inputs combined with large magnitudes of coastal carbon inputs appear to yield unrealistic DIC distributions (Figure 9d). It is important to keep in mind that the uncertainties associated with the prescribed residence times of terrestrial organic carbon would be intertwined with the uncertainties in coastal-open ocean exchange rates of carbon (Liu et al., 2019), which are not well represented in our coarse-resolution model.

To incorporate the uncertainty of the coastal margin carbon source stemming from the isotopic composition and lability of coastal margin carbon inputs to our estimates, we compute the difference between the simulated δ^{13}C-DIC and DIC from the perturbation simulations in Figure 9, and those of the optimized model. These differences were then added to the δ^{13}C-DIC and DIC from the 1,000 Monte Carlo simulations described in Section 5.2 (a subset of which are shown in Figure 8a), using random matching so that we obtain 1,000 new fields of δ^{13}C-DIC and DIC. Each of these fields is associated with a coastal margin carbon input that is equal to the coastal margin carbon input from the original Monte Carlo simulation, plus the coastal margin carbon input from the perturbation simulation (Figure 9) minus the coastal margin carbon input from the optimized model. These 1,000 new δ^{13}C-DIC fields are then assessed against the same criteria used

to select the models in Figure 8a, to determine which are consistent with the observational constraints. This selection yields 263 out of 1,000 members that are consistent with the specified criteria. The resulting probability distribution of coastal margin carbon inputs in these models (Figure 8b) is slightly wider than when the uncertainties stemming from the isotopic composition and lability of coastal margin carbon inputs are not considered (Figure 8a). Considering these additional uncertainties, terrestrial carbon inputs as low as 0.9 GtC/yr (a coastal margin carbon source of 0.3 GtC/yr) could be consistent with the carbon isotope observations (Figure 8b). Nonetheless, the magnitude of the terrestrial carbon inputs that corresponds to the highest probability remains nearly unchanged (Figure 8b).

5.4. Summary of Uncertainty Assessments

All of the uncertainty assessments and sensitivity experiments performed here (Figures 7–9) do not appear to affect the mean terrestrial carbon source of 1.4 PgC/yr (coastal margin input of 0.8 GtC/yr) derived from the optimized model, but they do indicate a wide range of uncertainty, with terrestrial carbon inputs ranging from ~0.9 GtC/yr to ~1.8 GtC/yr that could be consistent with the observed carbon isotope constraints. There are additional sources of uncertainty that were not fully explored above, including the influence of the SST (winter-like or annual average) used in the model due to its lack of seasonal cycle, the representation of organic carbon burial in the model, the potential for imbalances in the weathering and burial fluxes of organic and inorganic carbon, the formulation of the gas exchange parameterization for CO_2, and the representation of the industrial changes in coastal margin carbon inputs. We investigate these additional sources of uncertainty using a series of sensitivity experiments (see Text S2; Table S1), but none of these factors lead to inferred terrestrial carbon inputs outside the range already determined in the uncertainty analysis presented here. However, consideration of uncertainties in the model's representation of carbon burial in coastal sediments, as well as the potential for imbalances in the weathering and burial fluxes (Text S2) lead us to increase the uncertainty on the carbon burial fluxes to ±0.3 GtC/yr. Based on all of these assessments, we estimate a global terrestrial carbon input to the ocean of 1.4 ± 0.5 GtC/yr, which is balanced in the preindustrial era by a carbon burial of 0.2 ± 0.3 GtC/yr and a CO_2 outgassing of 1.2 ± 0.5 GtC/yr (Figure 10).

6. Summary and Conclusions

We used a numerical inverse model to estimate the terrestrial carbon inputs to the global ocean that are most consistent with a global database of stable carbon isotopes (Schmittner et al., 2017). We estimate that terrestrial carbon inputs to the global ocean of 1.4 ± 0.5 GtC/yr are needed to obtain consistency with the observed $\delta^{13}C$ of DIC (Figure 10). These inputs are larger than the prescribed riverine and airborne inputs of 0.6 GtC/yr, and also larger than the terrestrial carbon input of 0.9 GtC/yr adopted by the IPCC AR5 (Ciais et al., 2013). The excess carbon inputs of 0.8 ± 0.5 GtC/yr can be attributed to carbon export by SGD and from vegetation along coastal margins. These coastal margin carbon inputs have a $\delta^{13}C$ value of −26 ± 10‰ and occur predominantly in the Indian and Pacific Oceans. Terrestrial carbon inputs are balanced by a sedimentary burial of 0.2 ± 0.3 GtC/yr, and an efflux to the atmosphere of 1.2 ± 0.5 GtC/yr. Our model estimates a CO_2 efflux of 0.7 ± 0.5 GtC/yr in the open ocean and an anthropogenic CO_2 uptake of 2.1 GtC/yr as of the year 2000, for a net contemporary open-ocean air-sea CO_2 flux of 1.4 ± 0.5 GtC/yr (Figure 10). This agrees with independent observation-based estimates of the contemporary air-sea CO_2 flux (Landschützer et al. (2017); Landschützer et al., 2014; Rödenbeck et al., 2015). An estimated 0.5 ± 0.3 GtC/yr of CO_2 efflux occurs in the poorly resolved coastal ocean in our model, which combined with an anthropogenic CO_2 uptake of 0.2 GtC/yr gives a net efflux of 0.3 ± 0.3 GtC/yr as of 2000 (Figure 10). This CO_2 efflux is larger than suggested in some of previous studies, and suggests the need to carefully examine current CO_2 budgets in the land-ocean transition zone. In our model, 70% of the coastal efflux occurs in the tropics between 20°N and 20°S, particularly in the Indian and Pacific Oceans, which is precisely where observations are lacking in current data products (Laruelle et al., 2017). Nonetheless, we regard the carbon budget in the coastal zone as inconclusive due to the coarse model resolution and lack of representation of coastal processes.

Overall, this study suggests that coastal vegetated ecosystems, which are known to efficiently sequester a significant amount of atmospheric CO_2 (Bauer et al., 2013; Duarte, 2017), also rival inland watersheds in their contributions to lateral carbon transfers from land to marine ecosystems. This finding implies previ-

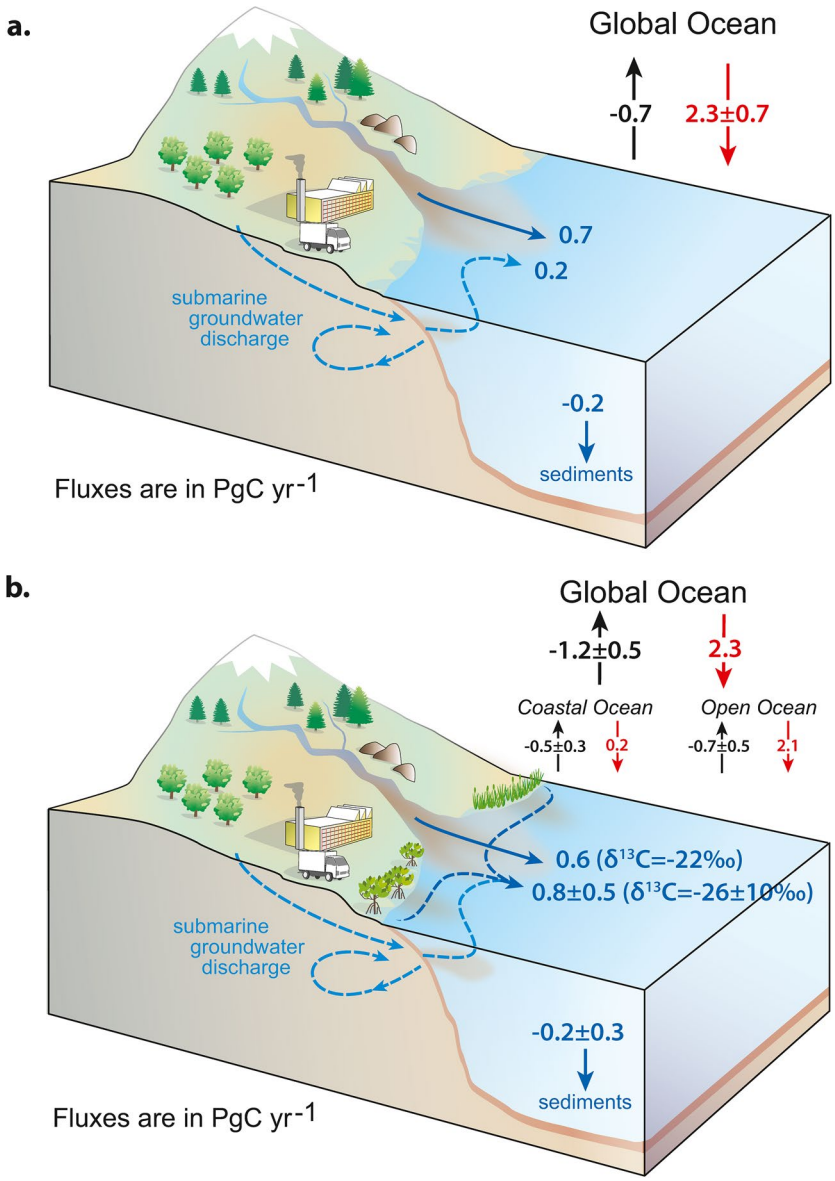

Figure 10. Schematic of the global carbon cycle. (a) Fluxes based on the IPCC AR5 (Ciais et al., 2013) with riverine and groundwater driven fluxes from Cole et al. (2007). (b) Fluxes based on this study. Riverine fluxes are prescribed using global databases (Mayorga et al., 2010; Meybeck & Ragu, 2012). Blue arrows and numbers indicate fluxes that are time-invariant from the preindustrial to industrial era. Black arrows and numbers indicate preindustrial efflux to the atmosphere, while red arrows and numbers indicate anthropogenic CO_2 uptake by the ocean as of the 2000s for (a) and 2000 for (b). The open ocean in (b) is defined as the open-ocean mask where the estimates based on oceanic pCO_2 measurements (Landschützer et al., 2017) are available, while the coastal ocean is defined as the remaining ocean area. The flux-weighted average for the terrestrial carbon $\delta^{13}C$ is shown in parenthesis next to the terrestrial carbon inputs.

ously overlooked climate sensitivities in the global carbon cycle: in addition to climate and hydrogeological factors on land, various oceanic factors including sea level rise and tides, as well as human activities such as coastal development, can impact coastal margin carbon fluxes. As coastal environments respond to climate change, understanding and predicting changes in the global carbon cycle will require models that can capture the multiple scales of interaction between ocean physics, coastal ecosystems, and coastal communities. Stable carbon isotopes will serve as important geochemical constraint on our understanding of the changing nature of carbon cycling between the terrestrial environment, coastal ecosystems, and the open ocean.

Data Availability Statement

The global database for the $\delta^{13}C$ of DIC is available at https://www.ncdc.noaa.gov/paleo-search/study/21750. The global database for PO_4 is available at https://www.nodc.noaa.gov/OC5/woa13/, and for alkalinity and $DI^{12}C$ at http://cdiac.ornl.gov/oceans/GLODAPv2/. The riverine carbon flux data used for model inputs are from http://staff.washington.edu/emiliom/globalnews/GlobalNEWS2ModeledExports_RH2000-version1.0.1.zip for organic carbon and https://doi.org/10.1594/PANGAEA.804574 for DIC. The atmospheric CO_2 and its isotopic composition data used for model forcing are from http://scrippsco2.ucsd.edu/data/atmospheric_co2/. The sea surface temperature data used in this study are from https://www.metoffice.gov.uk/hadobs/hadisst/data/download.html, https://www.esrl.noaa.gov/psd/data/gridded/data.noaa.ersst.v5.html, and https://www.esrl.noaa.gov/psd/data/gridded/data.cobe2.html. The wind data are from https://apps.ecmwf.int/datasets/data/interim-full-daily/levtype=sfc/. Our model outputs will be made available at https://climatedata.ibs.re.kr/data/papers/kwon-et-al-2021-gbc.

Acknowledgments
The authors thank those who have contributed to the global database of the water-column $\delta^{13}C$ of DIC and Andreas Schmittner for providing the database. The authors also thank E. Mayorga and A. Beusen for helping us find the riverine organic carbon input data, Gyu-Seok Lee for providing daily mean wind stress for a sensitivity experiment, and Jung-Eun Chu for helping us find the aerosol driven carbon input data. The authors also thank Ronald Benner for some references and helping E. Y. Kwon learn about land-derived carbon inputs to the ocean. Discussions with F. Primeau and K. Rodgers are also appreciated. The authors are grateful to Peter Raymond, Pierre Regnier, and anonymous reviewers for their inputs. E. Y. Kwon is funded by IBS-R028-D1 and NRF-2016R1D1A1B04931356. T. DeVries acknowledges support from NSF OCE-1948955.

References

Abril, G., Deborde, J., Savoye, N., Mathieu, F., Moreira-Turcq, P., Artigas, F., et al. (2013). Export of ^{13}C-depleted dissolved inorganic carbon from a tidal forest bordering the Amazon estuary. *Estuarine, Coastal and Shelf Science*, *129*, 23–27. https://doi.org/10.1016/j.ecss.2013.06.020

Alongi, D. M., & Mukhopadhyay, S. K. (2014). Contribution of mangroves to coastal carbon cycling in lowlatitude seas. *Agricultural and Forest Meteorology*, *213*, 266–272.

Anderson, T. R., Rowe, E. C., Polimene, L., Tipping, E., Evans, C. D., Barry, C. D. G., et al. (2019). Unified concepts for understanding and modelling turnover of dissolved organic matter from freshwaters to the ocean: The UniDOM model. *Biogeochemistry*, *146*, 105–123. https://doi.org/10.1007/s10533-019-00621-1

Bauer, J. E., Cai, W. J., Raymond, P. A., Bianchi, T. S., Hopkinson, C. S., & Regnier, P. A. (2013). The changing carbon cycle of the coastal ocean. *Nature*, *504*(7478), 61–70. https://doi.org/10.1038/nature12857

Becker, M., Steinhoff, T., & Körtzinger, A. (2018). A detailed view on the seasonality of stable carbon isotopes across the North Atlantic. *Global Bigeochemical Cycles*, *32*, 1406–1419. https://doi.org/10.1029/2018gb005905

Bianchi, D., Cui, X., Blair, N. E., Burdige, D. J., Eglinton, T., & Galy, V. (2017). Centers of organic carbon burial and oxidation at the land-ocean interface. *Organic Geochemistry*, *115*, 138–155. https://doi.org/10.1016/j.orggeochem.2017.09.008

Blair, N. E., & Aller, R. C. (2012). The fate of terrestrial organic carbon in the marine environment. *Annual Review of Marine Science*, *4*, 401–423. https://doi.org/10.1146/annurev-marine-120709-142717

Borges, A. V. (2005). Do we have enough pieces of the jigsaw to integrate CO_2 fluxes in the coastal ocean?. *Estuaries*, *28*, 3–27. https://doi.org/10.1007/bf02732750

Bourgeois, T., Orr, J. C., Resplandy, L., Terhaar, J., Ethé, C., Gehlen, M., & Bopp, L. (2016). Coastal-ocean uptake of anthropogenic carbon. *Biogeosciences*, *13*(14), 4167–4185. https://doi.org/10.5194/bg-13-4167-2016

Burton, M. R., & Sawyer, G. M. (2013). Deep carbon emissions from volcanoes. *Reviews in Mineralogy and Geochemistry*, *75*, 323–354. https://doi.org/10.2138/rmg.2013.75.11

Cai, W.-J. (2011). Estuarine and coastal ocean carbon paradox: CO2 sinks or sites of terrestrial carbon incineration?. *Annual Review of Marine Science*, *3*, 123–145. https://doi.org/10.1146/annurev-marine-120709-142723

Cartapanis, O., Galbraith, E. D., Bianchi, D., & Jaccard, S. (2018). Carbon burial in deep-sea sediment and implications for oceanic inventories of carbon and alkalinity over the last glacial cycle. *Climate of the Past*, *14*(11), 1819–1850. https://doi.org/10.5194/cp-2018-49

Chen, C.-T., Huang, T. H., Chen, Y.-C., Bai, Y., He, X., & Kang, Y. (2013). Air-sea exchanges of CO_2 in the world's coastal seas. *Biogeosciences*, *10*, 6509–6544. https://doi.org/10.5194/bg-10-6509-2013

Chen, X., Zhang, F., Lao, Y., Wang, X., Du, J., & Santos, I. R. (2018). Submarine groundwater discharge-derived carbon fluxes in mangroves: An important component of blue carbon budgets?. *Journal of Geophysical Research: Oceans*, *123*, 6962–6979. https://doi.org/10.1029/2018jc014448

Ciais, P., Sabine, C., Bala, G., Bopp, L., Brovkin, V., Canadell, J., et al. (2013). Carbon and other biogeochemical cycles. In T. F. Stocker, D. Qin, G.-K. Plattner, M. Tignor, S. K. Allen, J. Boschung, A. Nauels, Y. Xia, V. Bex, & P. M. Midgley (Eds.), *Climate change 2013: The physical science basis. Contribution of working group I to the fifth assessment report of the intergovernmental panel on climate change*. Cambridge University Press.

Cole, J. J., Prairie, Y. T., Caraco, N. F., McDowell, W. H., Tranvik, L. J., Striegl, R. G., et al. (2007). Plumbing the global carbon cycle: Integrating inland waters into the terrestrial carbon budget. *Ecosystems*, *10*, 171–184. https://doi.org/10.1007/s10021-006-9013-8

DeVries, T. (2014). The oceanic anthropogenic CO2 sink: Storage, air-sea fluxes, and transports over the industrial era. *Global Biogeochemical Cycles*, *28*, 631–647. https://doi.org/10.1002/2013gb004739

DeVries, T., & Primeau, F. (2011). Dynamically and observationally constrained estimates of water-mass distributions and ages in the global ocean. *Journal of Physical Oceanography*, *41*, 2381–2401. https://doi.org/10.1175/jpo-d-10-05011.1

Dorsett, A., Cherrier, J., Martin, J. B., & Cable, J. E. (2011). Assessing hydrologic and biogeochemical controls on pore-water dissolved inorganic carbon cycling in a subterranean estuary: A ^{14}C and ^{13}C mass balance approach. *Marine Chemistry*, *127*, 76–89. https://doi.org/10.1016/j.marchem.2011.07.007

Duarte, C. M. (2017). Reviews and syntheses: Hidden forests, the role of vegetated coastal habitats in the ocean carbon budget. *Biogeosciences*, *14*, 301–310. https://doi.org/10.5194/bg-14-301-2017

Eide, M., Olsen, A., Ninnemann, U. S., & Eldevik, T. (2017). A global estimate of the full oceanic ^{13}C Suess effect since the preindustrial. *Global Bigeochem. Cycles*, *31*, 492–514. https://doi.org/10.1002/2016gb005472

Freeman, K. H., & Hayes, J. M. (1992). Fractionation of carbon isotopes by phytoplankton and estimates of ancient CO_2 levels. *Global Biogeochemical Cycles*, *6*, 185–198. https://doi.org/10.1029/92gb00190

Galbraith, E. D., Kwon, E. Y., Bianchi, D., Hain, M. P., & Sarmiento, J. L. (2015). The impact of atmospheric pCO_2 on carbon isotope ratios of the atmosphere and ocean. *Global Biogeochemical Cycles*, *29*, 307–324. https://doi.org/10.1002/2014gb004929

Galy, V., Peucker-Ehrenbrink, B., & Eglinton, T. (2015). Global carbon export from the terrestrial biosphere controlled by erosion. *Nature*, *521*, 204–207. https://doi.org/10.1038/nature14400

Garcia, H. E., Locarnini, R. A., Boyer, T. P., Antonov, J. I., Maranova, O. K., Zweng, M. M., et al. (2014). World ocean atlas 2013. In S. Levitus (Ed.) *NOAA Atlas NESDIS 75 (Vol. 4)*. NOAA.

Goericke, R., & Fry, B. (1994). Variations of marine plankton $\delta^{13}C$ with latitude, temperature, and dissolved CO_2 in the world ocean. *Global Bigeochem. Cycles*, *8*, 85–90. https://doi.org/10.1029/93gb03272

Graven, H. D., Gruber, N., Key, R., Khatiwala, S., & Giraud, X. (2012). Changing controls on oceanic radiocarbon: New insights on shallow-to-deep ocean exchange and anthropogenic CO_2 uptake. *Journal of Geophysical Research*, *117*, C10005. https://doi.org/10.1029/2012jc008074

Gruber, N., Clement, D., Carter, B. R., Feely, R. A., van Heuven, S., Hoppema, M., et al. (2019). The oceanic sink for anthropogenic CO_2 from 1994 to 2007. *Science*, *363*(6432), 1193–1199. https://doi.org/10.1126/science.aau5153

Gruber, N., Gloor, M., Fletcher, M. S. E., Doney, S. C., Dutkiewicz, S., Follows, M. J., et al. (2009). Oceanic sources, sinks, and transport of atmospheric CO_2. *Global Biogeochemical Cycles*, *23*(GB1005). https://doi.org/10.1029/2008gb003349

Gruber, N., & Keeling, C. D. (2001). An improved estimate of the isotopic air-sea disequilibrium of CO_2: Implications for the oceanic uptake of anthropogenic CO_2. *Geophysical Research Letters*, *28*(3), 555–558. https://doi.org/10.1029/2000gl011853

Gruber, N., Keeling, C. D., Bacastow, R. B., Guenther, P. R., Lueker, T. J., Wahlen, M., et al. (1999). Spatiotemporal patterns of carbon-13 in the global surface oceans and the oceanis Suess effect. *Global Biogeochemical Cycles*, *13*, 307–335. https://doi.org/10.1029/1999gb900019

Gruber, N., Keeling, C. D., & Stocker, T. F. (1998). Carbon-13 constraints on the seasonal inorganic carbon budget at the BATS site in the northwestern Sargasso sea. *Deep-Sea Research I*, *45*, 673–717. https://doi.org/10.1016/s0967-0637(97)00098-8

Hedges, J. L., Keil, R. G., & Benner, R. (1997). What happens to terrestrial organic matter in the ocean?. *Organic Geochemistry*, *27*, 195–212. https://doi.org/10.1016/s0146-6380(97)00066-1

Hirahara, S., Ishii, M., & Fukuda, Y. (2014). Centennial-scale sea surface temperature analysis and its uncertainty. *Journal of Climate*, *27*, 57–75. https://doi.org/10.1175/jcli-d-12-00837.1

Huang, B., Thorne, P. W., Banzon, V. F., Boyer, T., Chepurin, G., Lawrimore, J. H., et al. (2017). Extended reconstructed sea surface temperature, version 5 (ERSSTv5): Upgrades, validations, and intercomparisons. *Journal of Climate*, *30*(20), 8179–8205. https://doi.org/10.1175/jcli-d-16-0836.1

Jahn, A., Lindsay, K., Giraud, X., Gruber, N., Otto-Bliesner, B. L., Liu, Z., & Brady, E. C. (2015). Carbon isotopes in the ocean model of the community earth system model (CESM1). *Geoscientific Model Development*, *8*(8), 2419–2434. https://doi.org/10.5194/gmd-8-2419-2015

Keeling, C. D., Piper, S. C., Bacastow, R. B., Wahlen, M., Whorf, T. P., Heimann, M., & Meijer, H. A. (2005). Atmospheric CO_2 and $^{13}CO_2$ exchange with the terrestrial biosphere and oceans from 1978 to 2000: Observations and carbon cycle implications. In J. R. Ehleringer, T. E. Cerling, & M. D. Dearing (Eds.), *A History of atmospheric CO2 and its effects on plants, animals, and ecosystems*. Springer Verlag.

Khatiwala, S., Tanhua, T., Milkaloff Fletcher, S., Gerber, M., Doney, S. C., Graven, H. D., et al. (2013). Global ocean storage of anthropogenic carbon. *Biogeosciences*, *10*, 2169–2191. https://doi.org/10.5194/bg-10-2169-2013

Krakauer, N. Y., Randerson, J. T., Primeau, F. W., Gruber, N.D.M, & (2006). Carbon isotope evidence for the latitudinal distribution and wind speed dependence of the air-sea gas transfer velocity. *Tellus*, *58B*, 390–417. https://doi.org/10.1111/j.1600-0889.2006.00223.x

Kwon, E. Y., Hain, M. P., Sigman, D. M., Galbraith, E. D., Sarmiento, J. L., & Toggweiler, J. R. (2012). North Atlantic ventilation of "southern-sourced" deep water in the glacial ocean. *Paleoceanography*, *27*(PA2208). https://doi.org/10.1029/2011pa002211

Kwon, E. Y., Kim, G., Primeau, F., Moore, W. S., Cho, H.-M., DeVries, T., et al. (2014). Global estimate of submarine groundwater discharge based on an observationally constrained radium isotope model. *Geophysical Research Letters*, *41*, 8438–8444. https://doi.org/10.1002/2014gl061574

Kwon, E. Y., & Primeau, F. (2008). Optimization and sensitivity of a global biogeochemistry ocean model using combined in situ DIC, alkalinity, and phosphate data. *Journal of Geophysical Research*, *113*(C08011). https://doi.org/10.1029/2007jc004520

Lacroix, F., Ilyina, T., & Hartmann, J. (2020). Oceanic CO_2 outgassing and biological production hotspots induced by pre-industrial river loads of nutrients and carbon in a global modeling approach. *Biogeosciences*, *17*, 55–88. https://doi.org/10.5194/bg-17-55-2020

Lagarias, J. C., Reeds, J. A., Wright, M. H., & Wright, P. E. (1998). Convergence properties of the Nelder-Mead simplex method in low dimensions. *SIAM Journal of Optimization*, *9*, 112–147. https://doi.org/10.1137/s1052623496303470

Lamarque, J. F., Bond, T. C., Eyring, V., Granier, C., Heil, A., Klimont, Z., et al. (2010). Historical (1850–2000) gridded anthropogenic and biomass burning emissions of reactive gases and aerosols: Methodology and application. *Atmospheric Chemistry and Physics*, *10*(15), 7017–7039. https://doi.org/10.5194/acp-10-7017-2010

Landschützer, P., Gruber, N., & Bakker, D. C. E. (2017). *An updated observation-based global monthly gridded sea surface pCO_2 and air-sea CO_2 flux product from 1982 through 2015 and its monthly climatology (NCEI Accession 0160558) Version 2.2 NOAA National Centers for Environmental Information. Dataset. [2017-07-11]*. NOAA National Centers for Environmental Information. https://www.ncei.noaa.gov/access/ocean-carbon-data-system/oceans/SPCO2_1982_2015_ETH_SOM_FFN.html

Landschützer, P., Gruber, N., Bakker, D. C. E., & Schuster, U. (2014). Recent variability of the global ocean carbon sink. *Global Biogeochemical Cycles*, *28*, 927–949. https://doi.org/10.1002/2014GB004853

Large, W. G., McWilliams, J. C., & Doney, S. C. (1994). Oceanic vertical mixing: A review and a model with nonlocal boundary layer parameterization. *Reviews of Geophysics*, *32*, 363–403. https://doi.org/10.1029/94rg01872

Laruelle, G. G., Cai, W.-J., Hu, X., Gruber, N., Mackenzie, F. T., & Regnier, P. (2018). Continental shelves as a variable but increasing global sink for atmospheric carbon dioxide. *Nature Communications*, *9*(454), 1–11. https://doi.org/10.1038/s41467-017-02738-z

Laruelle, G. G., Dürr, H. H., Lauerwald, R., Hartmann, J., Slomp, C. P., Goossens, N., & Regnier, P. A. G. (2013). Global multi-scale segmentation of continental and coastal waters from the watersheds to the continental margins. *Hydrology and Earth System Sciences*, *17*(5), 2029–2051. https://doi.org/10.5194/hess-17-2029-2013

Laruelle, G. G., Dürr, H. H., Slomp, C. P., & Borges, A. V. (2010). Evaluation of sinks and sources of CO_2 in the global coastal ocean using a spatially-explicit typology of estuaries and continental shelves. *Geophysical Research Letters*, *37*, L15607. https://doi.org/10.1029/2010gl043691

Laruelle, G. G., Landschutzer, P., Gruber, N., Tison, J.-L., Delille, B., & Regnier, P. (2017). Global high-resolution monthly pCO_2 climatology for the coastal ocean derived from neural network interpolation. *Biogeosciences*, *14*, 4545–4561. https://doi.org/10.5194/bg-14-4545-2017

Laruelle, G. G., Lauerwald, R., Pfeil, B., & Regnier, P. (2014). Regionalized global budget of the CO_2 exchange at the air-water interface in continental shelf seas. *Global Biogeochemical Cycles*, *28*, 1194–1214. https://doi.org/10.1002/2014gb004832

Lauvset, S. K., Key, R. M., Olsen, A., van Heuven, S., Velo, A., Lin, X., et al. (2016). A new global interior ocean mapped climatology: The 1° × 1° GLODAP version 2. *Earth System Science Data*, *8*(2), 325–340. https://doi.org/10.5194/essd-8-325-2016

Liu, X., Dunne, J. P., Stock, C. A., Harrison, M. J., Adcroft, A., & Resplandy, L. (2019). Simulating water residence time in the coastal ocean: A global perspective. *Geophysical Research Letters*, *46*, 13910–13919. https://doi.org/10.1029/2019gl085097

Ludwig, W., Amiotte-Suchet, P., & Probst, J. L. (1996). River discharges of carbon to the world's oceans: Determining local inputs of alkalinity and of dissolved and particulate organic carbon. *Sciences de la terre et des Planètes (Comptes Rendus de l'Académie des Sciences)*, *323*, 1007–1014.

Lynch-Stieglitz, J., Stocker, T. F., Broecker, W. S., & Fairbanks, R. G. (1995). The influence of air-sea exchange on the isotopic composition of oceanic carbon—observations and modeling. *Global Biogeochemical Cycles*, *9*, 653–665. https://doi.org/10.1029/95gb02574

MacFarling Meure, C., Etheridge, D., Trudinger, C., Steele, P., Langenfelds, R., van Ommen, T., et al. (2006). Law Dome CO_2, CH_4, and N_2O ice core records extended to 2000 years BP. *Geophysical Research Letters*, *33*(14). https://doi.org/10.1029/2006gl026152

Mackenzie, F. T., Lerman, A., & DeCarlo, E. H. (2011). Coupled C, N P, and O biogeochemical cycling at the land-ocean interface. In J. Middleburg, & R. Laane (Eds.), *Treatise on ocean and estuarine science*. Elsevier.

Maher, D. T., Call, M., Santos, I. R., & Sanders, C. J. (2018). Beyond burial: lateral exchange is a significant atmospheric carbon sink in mangrove forests. *Biology Letters*, *14*, 20180200. https://doi.org/10.1098/rsbl.2018.0200

Maher, D. T., Santos, I. R., Golsby-Smith, L., Gleeson, J., & Eyre, B. D. (2013). Groundwater-derived dissolved inorganic and organic carbon exports from a mangrove tidal creek: The missing mangrove carbon sink?. *Limnology & Oceanography*, *58*, 475–488. https://doi.org/10.4319/lo.2013.58.2.0475

Maier-Reimer, E., Mikolajewicz, U., & Hasselmann, K. (1993). Mean circulation of the Hamburg LSG OGCM and its sensitivity to the thermohaline surface forcing. *Journal of Physical Oceanography*, *23*, 731–757. https://doi.org/10.1175/1520-0485(1993)023<0731:mcothl>2.0.co;2

Manizza, M., Follows, M. J., Dutkiewicz, S., McClelland, J. W., Menemenlis, D., Hill, C. N., et al. (2009). Modeling transport and fate of riverine dissolved organic carbon in the Arctic Ocean. *Global Biogeochemical Cycles*, *23*, GB4006. https://doi.org/10.1029/2008gb003396

Marwick, T. R., Tamooh, F., Teodoru, C. R., Borges, A. V., Darchambeau, F., & Bouillon, S. (2015). The age of river-transported carbon: A global perspective. *Global Biogeochemical Cycles*, *29*, 122–137. https://doi.org/10.1002/2014gb004911

Mayorga, E., Seitzinger, S. P., Harrison, J. A., Dumont, E., Beusen, A. H. W., Bouwman, A. F., et al. (2010). Global nutrient export from waterSheds 2 (NEWS 2): Model development and implementation. *Environmental Modelling & Software*, *25*, 837–853. https://doi.org/10.1016/j.envsoft.2010.01.007

Meybeck, M. (1993). Riverine transport of atmospheric carbon: sources, global typology and budget. *Water, Air, and Soil Pollution*, *70*, 443–463. https://doi.org/10.1007/bf01105015

Meybeck, M., & Ragu, A. (2012). *GEMS-GLORI world river discharge database*. Laboratoire de Géologie Appliquée, Université Pierre et Marie Curie. https://doi.org/10.1594/PANGAEA.804574

Milliman, J. D. (1993). Production and accumulation of calcium carbonate in the ocean: Budget of a nonsteady state. *Global Biogeochemical Cycles*, *7*, 927–957. https://doi.org/10.1029/93gb02524

Moore, W. S. (2010). The effect of submarine groundwater discharge on the ocean. *Annual Review Marine Science*, *2*, 59–88. https://doi.org/10.1146/annurev-marine-120308-081019

Murgulet, D., Trevino, M., Douglas, A., Spalt, N., Hu, X., & Murgulet, V. (2018). Temporal and spatial fluctuations of groundwater-derived alkalinity fluxes to a semiarid coastal embayment. *The Science of the Total Environment*, *630*, 1343–1359. https://doi.org/10.1016/j.scitotenv.2018.02.333

Naegler, T., Ciais, P., Rodgers, K., & Levin, I. (2006). Excess radiocarbon constraints on air-sea gas exchange and the uptake of CO_2 by the oceans. *Geophysical Research Letters*, *33*, L11802. https://doi.org/10.1029/2005gl025408

Najjar, R. G., Jin, X., Louanchi, F., Aumont, O., Caldeira, K., Doney, S. C., et al. (2007). Impact of circulation on export production, dissolved organic matter, and dissolved oxygen in the ocean: Results from phase II of the ocean carbon-cycle model intercomparison project (OCMIP-2). *Global Biogeochemical Cycles*, *21*(3). https://doi.org/10.1029/2006gb002857

Peterson, B. J., & Fry, B. (1987). Stable isotopes in eco-system studies. *Annual Review of Ecology and Systematics*, *18*, 293–320. https://doi.org/10.1146/annurev.es.18.110187.001453

Polimene, L., Rivkin, R. B., Luo, Y.-W., Kwon, E. Y., Gehlen, M., Pena, M. A., et al. (2018). Modelling marine DOC degradation time scales. *National Science Review*, *5*, 468–474. https://doi.org/10.1093/nsr/nwy066

Popp, B. N., Takigiku, R., Hayes, J. M., Louda, J. W., & Baker, E. W. (1989). The post-Paleozoic chronology and mechanism of ^{13}C depletion in primary marine organic matter. *American Journal of Science*, *289*, 436–454. https://doi.org/10.2475/ajs.289.4.436

Quay, P., Sonnerup, R., Munro, D., & Sweeney, C. (2017). Anthropogenic CO_2 accumulation and uptake rates in the Pacific ocean based on changes in the $^{13}C/^{12}C$ of dissolved inorganic carbon. *Global Biogeochemical Cycles*, *31*, 59–80. https://doi.org/10.1002/2016gb005460

Quay, P., Sonnerup, R., Westby, T., Stutsman, J., & McNichol, A. (2003). Changes in the $^{13}C/^{12}C$ of dissolved inorganic carbon in the ocean as a tracer of anthropogenic CO_2 uptake. *Global Biogeochemical Cycles*, *17*(1004). https://doi.org/10.1029/2001gb001817

Racapé, V., Lo Monaco, C., Metzl, N., & Pierre, C. (2010). Summer and winter distribution of δ13C_DIC in surface waters of the south Indian ocean [20°S–60°S]. *Tellus B: Chemical and Physical Meteorology*, *62*(5), 660–673. https://doi.org/10.1111/j.1600-0889.2010.00504.x

Raymond, P. A. (2007). Flux and age of dissolved organic carbon exported to the Arctic ocean: A carbon isotopic study of the five largest Arctic rivers. *Global Biogeochemical Cycles*, *21*, GB4011. https://doi.org/10.1029/2007gb002934

Rayner, N. A., Parker, D. E., Horton, E. B., Folland, C. K., Alexander, L. V., Rowell, D. P., et al. (2003). Global analyses of sea surface temperature, sea ice, and night marine air temperature since the late nineteenth century. *Journal of Geophysical Research*, *108*(D14). https://doi.org/10.1029/2002JD002670

Regnier, P., Friedlingstein, P., Ciais, P., Mackenzie, F. T., Gruber, N., Janssens, I. A., et al. (2013). Anthropogenic perturbation of the carbon fluxes from land to ocean. *Nature Geoscience*, *9*, 597–607.

Resplandy, L., Keeling, C. D., Rödenbeck, C. C., Stephens, B. B., Khatiwala, S., Rodgers, K., et al. (2018). Revision of global carbon fluxes based on a reassessment of oceanic and riverine carbon transport. *Nature Geoscience*, *11*, 504–509. https://doi.org/10.1038/s41561-018-0151-3

Rödenbeck, C., Bakker, D. C. E., Gruber, N., Iida, Y., Jacobson, A. R., Jones, S., et al. (2015). Data-based estimates of the ocean carbon sink variability—first results of the surface ocean pCO_2 Mapping intercomparison (SOCOM). *Biogeosciences*, *12*(23), 7251–7278. https://doi.org/10.5194/bg-12-7251-2015

Rosentreter, J. A., Maher, D. T., Erler, D. V., Murray, R., & Eyre, B. D. (2018). Seasonal and temporal CO2 dynamics in three tropical mangrove creeks—A revision of global mangrove CO2 emissions. *Geochimica et Cosmochimica Acta*, *222*, 729–745. https://doi.org/10.1016/j.gca.2017.11.026

Rubino, M., Etheridge, D. M., Trudinger, C. M., Allison, C. E., Battle, M. O., Langenfelds, R. L., et al. (2013). A revised 1000 year atmospheric $\delta^{13}C$-CO_2 record from Law Dome and south Pole, Antarctica. *Journal of Geophysical Research: Atmospheres*, *118*, 8482–8499. https://doi.org/10.1002/jgrd.50668

Sabine, C. L., Feely, R. A., Gruber, N., Key, R., Lee, K., Bullister, J. L., et al. (2004). The ocean sink for anthropogenic CO_2. *Science*, *305*, 367–371. https://doi.org/10.1126/science.1097403

Sarmiento, J. L., & Gruber, N. (2006). *Ocean biogeochemical dynamics*. Princeton University Press.

Sarmiento, J. L., & Sundquist, E. T. (1992). Revised budget for the oceanic uptake of anthropogenic carbon dioxide. *Nature*, *356*, 589–593. https://doi.org/10.1038/356589a0

Schmittner, A., Bostock, H. C., Cartapanis, O., Curry, W. B., Filipsson, H. L., Galbraith, E. D., et al. (2017). Calibration of the carbon isotope composition ($\delta^{13}C$) of benthic foraminifera. *Paleoceanography*, *32*, 512–530. https://doi.org/10.1002/2016pa003072

Schmittner, A., Gruber, N., Mix, A. C., Key, R. M., Tagliabue, A., & Westberry, T. K. (2013). Biology and air-sea gas exchange controls on the distribution of carbon isotope ratios ($\delta^{13}C$) in the ocean. *Biogeosciences*, *10*, 5793–5816. https://doi.org/10.5194/bg-10-5793-2013

Sonnerup, R. E., McNichol, A. P., Quay, P., Gammon, R. H., Bullister, J. L., Sabine, C., & Slater, R. D. (2007). Anthropogenic $\delta^{13}C$ changes in the north Pacific ocean reconstructed using a multiparameter mixing approach (MIX). *Tellus*, *59B*, 303–317. https://doi.org/10.1111/j.1600-0889.2007.00250.x

Sonnerup, R., & Quay, P. D. (2012). ^{13}C constraints on ocean carbon cycle models. *Global Bigeochem. Cycles*, *26*, GB2014. https://doi.org/10.1029/2010gb003980

Sweeney, C., Gloor, E., Jacobson, A. R., Key, R. M., McKinley, G., Sarmiento, J. L., & Wanninkhof, R. (2007). Constraining global air-sea gas exchange for CO_2 with recent bomb ^{14}C measurements. *Global Biogeochemical Cycles*, *21*, GB2015. https://doi.org/10.1029/2006gb002784

Szymczycha, B., Maciejewska, A., Winogradow, A., & Pempkowiak, J. (2014). Could submarine groundwater discharge be a significant carbon source to the southern Baltic Sea?. *Oceanologia*, *56*, 327–347. https://doi.org/10.5697/oc.56-2.327

Taniguchi, M., Burnett, W. C., Cable, J. E., & Turner, J. V. (2002). Investigation of submarine groundwater discharge. *Hydrological Processes*, *16*, 2115–2129. https://doi.org/10.1002/hyp.1145

Tans, P. P., Berry, J. A., & Keeling, R. F. (1993). Oceanic $^{12}C/^{13}C$ observations: A new window on ocean CO_2 uptake. *Global Biogeochemical Cycles*, *7*(2), 353–368. https://doi.org/10.1029/93gb00053

Wanninkhof, R. (1992). Relationship between wind-speed and gas exchange over the ocean. *Journal of Geophysical Research*, *97*, 7373–7382. https://doi.org/10.1029/92jc00188

Wanninkhof, R., Park, G.-H., Tankahashi, T., Sweeney, C., Feely, R. A., Nojiri, Y., et al. (2013). Global ocean carbon uptake: Magnitude, variability and trends. *Biogeosciences*, *10*, 1983–2000. https://doi.org/10.5194/bg-10-1983-2013

Watson, A. J., Schuster, U., Shutler, J. D., Holding, T., Ashton, I. G. C., Landschützer, P., et al. (2020). Revised estimates of ocean-atmosphere CO_2 flux are consistent with ocean carbon inventory. *Nature Communications*, *11*(4422). https://doi.org/10.1038/s41467-020-18203-3

Zhang, J., Quay, P. D., & Wilbur, D. O. (1995). Carbon-isotope fractionation during gas-water exchange and dissolution of CO_2. *Geochimica et Cosmochimica Acta*, *59*, 107–114. https://doi.org/10.1016/0016-7037(95)91550-d